

<sup>1</sup> MPMICE: A hybrid MPM-CFD model for simulating  
<sup>2</sup> coupled problems in porous media. Application to  
<sup>3</sup> earthquake-induced submarine landslides

<sup>4</sup> Quoc Anh Tran<sup>a,b</sup>, Gustav Grimstad<sup>a</sup>, Seyed Ali Ghoreishian Amiri<sup>a</sup>

<sup>a</sup>*Norwegian University of Science and Technology, , Trondheim, 7034, Norway*

<sup>b</sup>*quoc.a.tran@ntnu.no*

---

<sup>5</sup> **Abstract**

<sup>6</sup> In this paper, we describe a soil-fluid-structure interaction model that com-  
<sup>7</sup> bines soil mechanics (saturated sediments), fluid mechanics (seawater or air),  
<sup>8</sup> and solid mechanics (structures). The formulation combines the Material  
<sup>9</sup> Point Method, which models large deformation of the porous media and the  
<sup>10</sup> structure, with the Implicit Continuous-fluid Eulerian, which models com-  
<sup>11</sup> plex fluid flows. We validate the model and simulate the whole process of  
<sup>12</sup> earthquake-induced submarine landslides. We show that this model captures  
<sup>13</sup> complex interactions between saturated sediment, seawater, and structure,  
<sup>14</sup> so we can use the model to estimate the impact of potential submarine land-  
<sup>15</sup> slides on offshore structures.

<sup>16</sup> *Keywords:*

<sup>17</sup> Material Point Method, MPMICE, submarine landslide.

---

<sup>18</sup> **Contents**

<sup>19</sup> <b>Nomenclature</b>	<sup>4</sup>
<sup>20</sup> <b>Introduction</b>	<sup>6</sup>
<sup>21</sup> <b>Theory and formulation</b>	<sup>9</sup>
<sup>22</sup> Assumptions . . . . .	<sup>9</sup>
<sup>23</sup> Governing equations . . . . .	<sup>9</sup>
<sup>24</sup> Constitutive soil model . . . . .	<sup>11</sup>
<sup>25</sup> Turbulent model . . . . .	<sup>12</sup>
<sup>26</sup> Frictional force for soil-structure interaction . . . . .	<sup>13</sup>
<sup>27</sup> Momentum and Energy exchange model . . . . .	<sup>13</sup>
<sup>28</sup> Solving momentum and energy exchange with an implicit solver	<sup>15</sup>
<sup>29</sup> Equation of state for fluid phases . . . . .	<sup>16</sup>
<sup>30</sup> <b>Numerical implementation</b>	<sup>17</sup>
<sup>31</sup> Interpolation from Solid Particle to Grid . . . . .	<sup>18</sup>
<sup>32</sup> Compute equation of state for fluid phase . . . . .	<sup>20</sup>
<sup>33</sup> Compute cell face velocity . . . . .	<sup>20</sup>
<sup>34</sup> Compute cell face temperature . . . . .	<sup>21</sup>
<sup>35</sup> Compute fluid pressure (implicit scheme) . . . . .	<sup>22</sup>
<sup>36</sup> Compute viscous shear stress term of the fluid phase . . . . .	<sup>22</sup>
<sup>37</sup> Compute nodal internal temperature of the solid phase . . . . .	<sup>23</sup>
<sup>38</sup> Compute and integrate acceleration of the solid phase . . . . .	<sup>23</sup>
<sup>39</sup> Compute Lagrangian value (mass, momentum and energy) . . . . .	<sup>23</sup>
<sup>40</sup> Compute Lagrangian specific volume of the fluid phase . . . . .	<sup>25</sup>
<sup>41</sup> Compute advection term and advance in time . . . . .	<sup>25</sup>
<sup>42</sup> Interpolate from cell to node of the solid phase . . . . .	<sup>26</sup>
<sup>43</sup> Update the particle variables . . . . .	<sup>26</sup>
<sup>44</sup> <b>Numerical validation</b>	<sup>27</sup>
<sup>45</sup> Fluid Flow through isothermal porous media . . . . .	<sup>27</sup>
<sup>46</sup> Isothermal consolidation . . . . .	<sup>28</sup>
<sup>47</sup> Thermal induced cavity flow . . . . .	<sup>29</sup>
<sup>48</sup> <b>Numerical examples</b>	<sup>31</sup>
<sup>49</sup> Underwater debris flow . . . . .	<sup>31</sup>
<sup>50</sup> Validation of soil response to the seismic loading . . . . .	<sup>34</sup>

51	Earthquake-induced submarine landslides . . . . .	37
52	<b>Conclusions</b>	41
53	<b>Acknowledgements</b>	42
54	<b>Data Availability Statement</b>	42
55	<b>Appendix: Equation derivation</b>	42
56	Evolution of porosity . . . . .	43
57	Momentum conservation . . . . .	43
58	Energy conservation . . . . .	44
59	Advanced Fluid Pressure . . . . .	45
60	Momentum and Energy exchange with an implicit solver . . . . .	46

<sup>61</sup> **Nomenclature**

**General variables**

<u>Variable</u>	<u>Dimensions</u>	<u>Description</u>
$V$	$[L^3]$	Representative volume
$n$		Porosity
$\sigma$	$[ML^{-1}t^{-2}]$	Total stress tensor
$\Delta t$	$[t]$	Time increment
$\mathbf{b}$	$[ML^1t^{-2}]$	Body force
$c_v$	$[L^2t^{-2}T^{-1}]$	Constant volume specific heat
$f_d$	$[MLt^{-2}]$	Drag forces in momentum exchange term
$f^{int}$	$[MLt^{-2}]$	Internal forces
$f^{ext}$	$[MLt^{-2}]$	External forces
$q_{fs}$	$[MLt^{-2}]$	Heat exchange term
$S$		Weighting function
$\nabla S$		Gradient of weighting function

<sup>62</sup>

**Solid phase**

<u>Variable</u>	<u>Dimensions</u>	<u>Description</u>
$m_s$	$[M]$	Solid mass
$\rho_s$	$[ML^{-3}]$	Solid density
$\phi_s$		Solid volume fraction
$\bar{\rho}_s$	$[ML^{-3}]$	Bulk Solid density
$\mathbf{x}_s$	$[L]$	Solid Position vector
$\mathbf{U}_s$	$[Lt^{-1}]$	Solid Velocity vector
$\mathbf{a}_s$	$[Lt^{-2}]$	Solid Acceleration vector
$\sigma'$	$[ML^{-1}t^{-2}]$	Effective Stress tensor
$\epsilon$		Strain tensor
$e_s$	$[L^2t^{-2}]$	Solid Internal energy per unit mass
$T_s$	$[T]$	Solid Temperature
$\mathbf{F}_s$		Solid Deformation gradient
$V_s$	$[L^3]$	Solid Volume

**Fluid phase**

<u>Variable</u>	<u>Dimensions</u>	<u>Description</u>
$m_f$	[M]	Fluid mass
$\rho_f$	[ML <sup>-3</sup> ]	Fluid density
$\phi_f$		Fluid volume fraction
$\bar{\rho}_f$	[ML <sup>-3</sup> ]	Bulk Fluid density
$\mathbf{U}_f$	[Lt <sup>-1</sup> ]	Fluid Velocity vector
$\boldsymbol{\sigma}_f$	[ML <sup>-1</sup> t <sup>-2</sup> ]	Fluid stress tensor
$p_f$	[ML <sup>-1</sup> t <sup>-2</sup> ]	Fluid isotropic pressure
$\boldsymbol{\tau}_f$	[ML <sup>-1</sup> t <sup>-2</sup> ]	Fluid shear stress tensor
$e_f$	[L <sup>2</sup> t <sup>-2</sup> ]	Fluid Internal energy per unit mass
$T_f$	[T]	Fluid Temperature
$v_f$	[L <sup>3</sup> /M]	Fluid Specific volume $\frac{1}{\rho_f}$
$\alpha_f$	[1/T]	Thermal expansion
$\mu$	[ML <sup>-1</sup> t <sup>-1</sup> ]	Fluid viscosity
$V_f$	[L <sup>3</sup> ]	Fluid Volume

**Superscript**

<u>Variable</u>	<u>Dimensions</u>	<u>Description</u>
$n$		Current time step
$L$		Lagrangian values
$n + 1$		Next time step

**Subscript**

$c$	Cell-centered quantity
$p$	Particle quantity
$i$	Node quantity
$FC$	Cell face quantity
$L, R$	Left and Right cell faces

64 **Introduction**

65 Many geological natural processes and their interactions with man-made  
66 structures are influenced by soil-fluid-structure interactions. The prediction  
67 of these processes requires a tool that can capture complex interactions  
68 between soil, fluid, and structure, such as the process of submarine land-  
69 slides. Indeed, The offshore infrastructure as well as coastal communities  
70 may be vulnerable to submarine landslides. Submarine landslides contain  
71 three stages: triggering, failure, and post-failure. Erosion or earthquakes can  
72 trigger slope failures in the first stage. Following the failure, sediments move  
73 quickly after the post-failure stage. In other words, solid-like sediments will  
74 behave like a fluid after failure. This transition, where the sediment trans-  
75 forms into fluid-like debris and then re-establishes a porous medium, poses  
76 a challenging task for simulating submarine landslides.

77 Due to this transition, submarine landslides can be modeled using either the  
78 Eulerian framework or the Lagrangian framework. The Eulerian framework  
79 involves the calculation of material response at specific time-space points.  
80 For instance, methods within Computational Fluid Dynamics, for example  
81 using Finite Volume Methods (FVM) are employed to simulate submarine  
82 landslides [1, 2, 3, 4] by solving governing equations in a full-Eulerian frame-  
83 work. While FVM is capable of handling complex flows, such as turbulent  
84 flows, it falls short of accounting for the triggering mechanisms of subma-  
85 rine landslides. This is due to the challenge of incorporating 'constitutive  
86 laws' of sediment materials within the Eulerian framework. This is particu-  
87 larly significant because converting material time derivatives into fixed space  
88 derivatives involves arduous mathematical tasks, especially for soil materials  
89 that rely on nonlinear tensor operations and history-dependent state/internal  
90 variables. In contrast, the Lagrangian framework, including various particle-  
91 based methods, provides a solution to this problem. In the Lagrangian frame-  
92 work, material "particles" are tracked individually through space, and ma-  
93 terial properties and internal variables are determined at and follow these  
94 particles. These methods have been extensively used to simulate landslides,  
95 like Material Point Method (MPM) [5], Smooth Particle Hydro Dynamics [6],  
96 Particle Finite Element Method [7], or Coupled Eulerian-Lagrangian Method  
97 [8]. For simplicity, these previous simulations have adopted a total stress  
98 analysis, neglecting the pore pressure development which is a key factor trig-  
99 gering slope failures.

100 Recent advancements in particle-based Lagrangian methods have allowed for

the modeling of fluid flows in porous media using sets of Lagrangian particles. Within the MPM family, there is a specific approach known as double-point MPM [9, 10, 11]. In this method, fluid particles and solid particles are overlaid within a single computational grid. However, it is important to note that particle-based methods encounter numerical instability when modeling fluid flows. To address this, various numerical techniques are employed, including the B-bar method [9], null-space filter [12], or least square approximation [13, 14]. These methods are necessary, especially when dealing with complex and turbulent fluid flows, such as those seen in submarine landslides. In such scenarios, Eulerian methods like FVM/CFD are preferred due to their computational efficiency, particularly when turbulence occurs at fine resolutions. CFD has even been employed in combination with the Discrete Element Method [15, 16] to study granular grain - fluid interactions, allowing for the examination of micro-scale behavior and realistic grain morphology. However, the computational demands of Discrete Element Methods can be quite challenging when applied to practical scenarios. Therefore, an ideal approach might involve the integration of CFD with particle-based continuum methods. Additionally, MPM can also be coupled with thermal effects [17, 18, 19], opening up the possibility of capturing hydro-thermal-mechanical coupling. Over the past two decades, more than 50 particle-based methods have been developed to address the simulation of large deformations in solids [20]. Among these, MPM emerges as a strong candidate for coupling with CFD. This is because MPM incorporates a stationary mesh during computation, just like CFD. As such, MPM and CFD can be seamlessly integrated within a unified computational mesh, offering a promising approach for tackling complex fluid-solid interactions.

A numerical method for simulating soil-fluid-structure interaction (Figure 1) involving large deformations, is presented in this work in order to simulate the interaction between sediment (soil), seawater (fluid) and offshore structures (structure) namely MPMICE (Figure 2). In the MPMICE, the Material Point Method (MPM) is coupled with the Implicit Continuous Eulerian (ICE) [21]. The MPM method is a particle method that allows the porous soil to undergo arbitrary distortions. The ICE method, on the other hand, is a conservative finite volume technique with all state variables located at the cell center (temperature, velocity, mass, pressure). The ICE method offers certain advantages in comparison to conventional FVM in the realm of flow computation encompassing all velocity ranges. An initial technical report [22] at Los Alamos National Laboratory provided the theoretical and

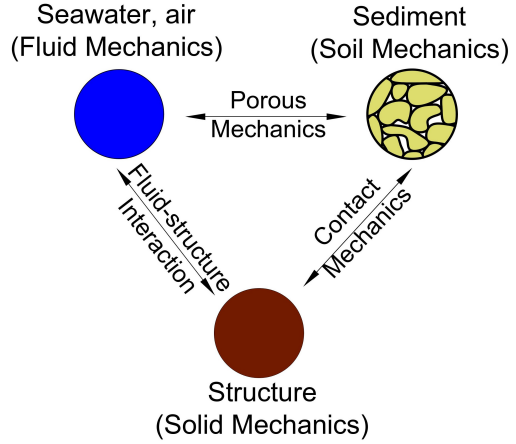


Figure 1: Interaction between soil-fluid-structure

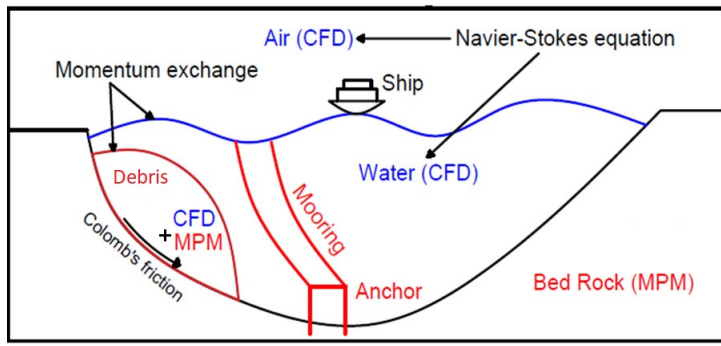


Figure 2: Coupling of soil-water-structure interaction using MPMICE

139 algorithmic foundation for the MPMICE, followed by the MPMICE development  
 140 and implementation in the high-performance Uintah computational  
 141 framework for simulating fluid-structure interactions [23]. This paper pri-  
 142 marily contributes further to the development of the MPMICE for analyzing  
 143 the **soil**-fluid-structure interaction, since sediment should be considered as a  
 144 porous media (soil) and not as a solid to capture the evolution of the pore  
 145 water pressure. Baumgarten et al. [24] made the first attempt at coupling  
 146 the FVM with the MPM for the simulation of soil-fluid interaction by us-  
 147 ing an explicit time integration for the single-phase flow. In contrast to the  
 148 mentioned work, we use implicit time integration for the multi phase flows.

149 **Theory and formulation**

150 This section lay out the theoretical framework for the MPMICE model.  
151 We use the common notation of the continuum mechanics with vector and  
152 tensor denoted simply by using bold font and scalar denoted by using normal  
153 font. The notation are shown in Nomenclature.

154 **Assumptions**

155 The following assumptions are made for the MPMICE model.

- 156 1. Solid phases (MPM) are described in a Lagrangian formulation while  
157 fluid phases (ICE) are described in an Eulerian formulation in the  
158 framework of continuum mechanics and mixture theory.  
159 2. Solid grains are incompressible while the fluid phases are compressible.  
160 3. There is no mass exchange between solid and fluid phases.  
161 4. Terzaghi's effective stress is valid.

162 **Governing equations**

163 A representative element volume  $\Omega$  is decomposed by two domains: solid  
164 domains  $\Omega_s$  and fluid domains  $\Omega_f$ . Then, all domains are homogenized  
165 into two overlapping continua. Considering the volume fraction of solid  
166  $\phi_s = \Omega_s/\Omega$  and fluid  $\phi_f = \Omega_f/\Omega$  with the true (or Eulerian) porosity  
167  $n = \sum \phi_f$  of the representative element volume, the average density of solid  
168 and fluid phases are defined as:

169

$$\bar{\rho}_s = \phi_s \rho_s, \quad \bar{\rho}_f = \phi_f \rho_f \quad (1)$$

170 The mass of solid and fluid phases are:

171

$$m_s = \int_{\Omega_s} \rho_s dV = \bar{\rho}_s V, \quad m_f = \int_{\Omega_f} \rho_f dV = \bar{\rho}_f V \quad (2)$$

172 Reviewing the Terzaghi's effective stress concept for the saturated porous  
173 media, the total stress  $\boldsymbol{\sigma}$  is calculated by:

174

$$\boldsymbol{\sigma} = \boldsymbol{\sigma}' - p_f \mathbf{I} \quad (3)$$

175 The balance equations are derived based on the mixture theory. The rep-  
176 resentative thermodynamic state of the fluid phases are given by the vector  
177  $[m_f, \mathbf{U}_f, e_f, T_f, v_f]$  which are mass, velocity, internal energy, temperature,

178 specific volume. The representative state of the solid phases are given by the  
 179 vector  $[m_s, \mathbf{U}_s, e_s, T_s, \boldsymbol{\sigma}', p_f]$  which are mass, velocity, internal energy, temper-  
 180 ature, effective stress and pore water pressure. The derivation is presented  
 181 in detail in the Appendix.

182

---

### 183 Mass Conservation

184 The mass balance equations for both fluid (e.g., water, air) and solid phases  
 185 are:

186

$$\frac{1}{V} \frac{\partial m_f}{\partial t} + \nabla \cdot (m_f \mathbf{U}_f) = 0, \frac{1}{V} \frac{D_s m_s}{Dt} = 0 \quad (4)$$

187 Solving the mass balance equation of the solid phase leads to:

$$\frac{D_s n}{Dt} = \phi_s \nabla \cdot \mathbf{U}_s \quad (5)$$

188

---

### 189 Momentum Conservation

190 The momentum balance equations for each fluid phases (e.g., water, air) are:

$$\frac{1}{V} \left[ \frac{\partial(m_f \mathbf{U}_f)}{\partial t} + \nabla \cdot (m_f \mathbf{U}_f \mathbf{U}_f) \right] = -\phi_f \nabla p_f + \nabla \cdot \boldsymbol{\tau}_f + \bar{\rho}_f \mathbf{b} + \sum \mathbf{f}_d \quad (6)$$

191 The momentum balance equations for each solid phases are:

$$\frac{1}{V} \frac{D_s(m_s \mathbf{U}_s)}{Dt} = \nabla \cdot (\boldsymbol{\sigma}') - \phi_s \nabla p_f + \bar{\rho}_s \mathbf{b} + \sum \mathbf{f}_{fric} - \sum \mathbf{f}_d \quad (7)$$

192

---

### 193 Energy Conservation

194 The internal energy balance equations for each fluid phases (e.g., water, air)  
 195 are:

$$\frac{1}{V} \left[ \frac{\partial(m_f e_f)}{\partial t} + \nabla \cdot (m_f e_f \mathbf{U}_f) \right] = -\bar{\rho}_f p_f \frac{D_f v_f}{Dt} + \boldsymbol{\tau}_f : \nabla \mathbf{U}_f + \nabla \cdot \mathbf{q}_f + \sum q_{sf} \quad (8)$$

196 The internal energy balance equations for each solid phases are:

$$\frac{m_s}{V} c_v \frac{D_s(T_s)}{Dt} = \boldsymbol{\sigma}' : \frac{D_s(\boldsymbol{\epsilon}_s^p)}{Dt} + \nabla \cdot \mathbf{q}_s - \sum q_{sf} \quad (9)$$

197 where  $c_v$  is the specific heat at constant volume of the solid materials.

198

---

199 Closing the systems of equations, the following additional models are needed:  
 200 (1) A constitutive equation to describe the stress - strain behaviour of solid  
 201 phase (computing effective stress  $\sigma'$ ).  
 202 (2) Optional turbulent model to compute the viscous shear stress  $\tau_f$ .  
 203 (3) Frictional forces  $\mathbf{f}_{fric}$  for the contact for soil-structure interaction be-  
 204 tween solid/porous materials with the friction coefficient  $\mu_{fric}$ .  
 205 (4) Exchange momentum models (computing drag force  $\mathbf{f}_d$ ) for interaction  
 206 between materials.  
 207 (5) Energy exchange models (computing temerature exhange term  $q_{sf}$ ) for  
 208 interaction between materials.  
 209 (6) An equation of state to establish relations between thermodynamics vari-  
 210 ables of each fluid materials  $[P_f, \bar{\rho}_f, v_f, T_f, e_f]$ .  
 211 (7) Thermal conduction model to compute thermal flux of solid phase  $\mathbf{q}_s$  and  
 212 liquid phase  $\mathbf{q}_s$ .  
 213 Four thermodynamic relations for the equation of states are:

$$\begin{aligned}
 e_f &= e_f(T_f, v_f) \\
 P_f &= P_f(T_f, v_f) \\
 \phi_f &= v_f \bar{\rho}_f \\
 0 &= n - \sum_{f=1}^{N_f} v_f \bar{\rho}_f
 \end{aligned} \tag{10}$$

214 *Constitutive soil model*

215 As a result of the explicit MPM formulation, we can derive the consti-  
 216 tutive law in the updated Lagrangian framework of "small strain - large  
 217 deformation". Therefore, the rotation of the particles (representative ele-  
 218 ment volume) is manipulated by rotating the Cauchy stress tensor. First,  
 219 the deformation gradient is decomposed into the polar rotation tensor  $\mathbf{R}_s^{n+1}$   
 220 and stretch tensor  $\mathbf{V}_s^{n+1}$  as:

$$\mathbf{F}_s^{n+1} = \mathbf{V}_s^{n+1} \mathbf{R}_s^{n+1} \tag{11}$$

221 Then, before calling the constitutive model, the stress and strain rate tensor  
 222 are rotated to the reference configuration as:

$$\boldsymbol{\sigma}'^{n*} = (\mathbf{R}_s^{n+1})^T \boldsymbol{\sigma}'^n \mathbf{R}_s^{n+1} \tag{12}$$

$$\delta\boldsymbol{\epsilon}^{n*} = (\mathbf{R}_s^{n+1})^T \delta\boldsymbol{\epsilon}^n \mathbf{R}_s^{n+1} \tag{13}$$

224 Using the constitutive model with the input tensors  $\sigma'^{n*}, \delta\epsilon^{n*}$  to compute  
 225 the Cauchy stress tensor at the advanced time step  $\sigma'^{n+1*}$  then rotating it  
 226 back to current configuration as:

$$\sigma'^{n+1} = R_s^{n+1} \sigma'^{n+1*} (R_s^{n+1})^T \quad (14)$$

227 In this paper, we adopt the hyper-elastic Neo Hookean model for the structure  
 228 materials and additionally Mohr-Coulomb failure criteria for the soil (porous  
 229 media) materials. The Cauchy stress of the hyper-elastic Neo Hookean model  
 230 can be written as:

$$\sigma' = \frac{\lambda \ln(J)}{J} + \frac{\mu}{J} (\mathbf{F}\mathbf{F}^T - \mathbf{J}) \quad (15)$$

231 where  $\lambda$  and  $\mu$  are bulk and shear modulus ad  $J$  is the determinant of the  
 232 deformation gradient  $\mathbf{F}$ . And the yield function  $f$  and flow potentials  $g$  of  
 233 the Mohr-Coulomb can be written as:

$$\begin{aligned} f &= -\sigma'_1 + \sigma'_3 + 2c' \cos(\phi') + (\sigma'_1 + \sigma'_3) \sin(\phi') \\ g &= -\sigma'_1 + \sigma'_3 + 2c' \cos(\psi') + (\sigma'_1 + \sigma'_3) \sin(\psi') \end{aligned} \quad (16)$$

234 In the equations,  $c'$ ,  $\phi'$ , and  $\psi'$  represent the cohesion, friction angle, and  
 235 dilation angle, respectively.  $\sigma'_1$  and  $\sigma'_3$  denote the maximum and minimum  
 236 principal stresses, with the condition  $\sigma'_1 < \sigma'_3 < 0$ . It is important to note  
 237 that in our assumptions, stress is considered positive during extension, which  
 238 means the signs of the stresses in these equations are opposite to those in  
 239 standard Soil Mechanic's textbooks. The numerical implementation follows  
 240 the approach described in Clausen et al. [25].

#### 241 *Turbulent model*

242 The turbulent effect is modelled using a statistical approach namely large-  
 243 eddy simulation. In this approach, the micro-scale turbulent influence in the  
 244 dynamics of the macro-scale motion is computed through simple models like  
 245 Smagorinsky model [26]. In the Smagorinsky model, the residual stress tensor  
 246 is:

$$\tau_{ij} = 2\mu_{eff}(\bar{S}_{ij} - \frac{1}{3}\delta_{ij}\bar{S}_{kk}) + \frac{1}{3}\delta_{ij}\tau_{kk} \quad (17)$$

247 where the the strain rate tensor is given by:

$$\bar{S}_{ij} = \frac{1}{2}(\frac{\delta \bar{\mathbf{U}}_i}{\delta x_j} + \frac{\delta \bar{\mathbf{U}}_j}{\delta x_i}) \quad (18)$$

<sup>248</sup> and the effective viscosity is sum of molecular viscosity and turbulent viscos-  
<sup>249</sup> ity  $\mu_{eff} = \mu + \mu_t$  in which the turbulent viscosity  $\mu_t$  is calculated by:

$$\mu_t = (C_s \Delta)^2 \sqrt{2\bar{S}_{ij}\bar{S}_{ij}} \quad (19)$$

<sup>250</sup> where  $C_s$  is the Smagorinsky constant with the value of 0.1 and  $\Delta = \sqrt[3]{dxdydz}$   
<sup>251</sup> is the grid size that defines the subgrid length scale.

<sup>252</sup> *Frictional force for soil-structure interaction*

<sup>253</sup> MPMICE includes a contact law for the interaction between soil and  
<sup>254</sup> structure using the first Coulomb friction contact for MPM presented by  
<sup>255</sup> Bardenhagen et al. [27]. The magnitude of the friction force at the contact  
<sup>256</sup> depends on the friction coefficient  $\mu_{fric}$  and the normal force  $\mathbf{f}_{norm}$  computed  
<sup>257</sup> from the projection of the contact force in the normal direction.

$$\mathbf{f}_{fric} = \mu_{fric} \mathbf{f}_{norm} \quad (20)$$

<sup>258</sup> The contact determines whether the soil is sliding or sticking to the structure  
<sup>259</sup> by comparing the friction force with the sticking force  $\mathbf{f}_{stick}$  can be computed  
<sup>260</sup> from the projection of the contact force in the tangent direction as:

$$\begin{aligned} & \text{if } \mathbf{f}_{fric} \geq \mathbf{f}_{stick} \text{ no sliding} \\ & \text{if } \mathbf{f}_{fric} < \mathbf{f}_{stick} \text{ sliding occurs} \end{aligned} \quad (21)$$

<sup>261</sup> Frictional sliding between solid materials also generates dissipation and the  
<sup>262</sup> work rate generated from the sliding can be calculated as:

$$\Delta W_{friction} = \mathbf{f}_{fric} d \quad (22)$$

<sup>263</sup> where  $d$  is the sliding distance which can be computed based on the sliding  
<sup>264</sup> velocity between two materials.

<sup>265</sup> *Momentum and Energy exchange model*

<sup>266</sup> Currently, the energy exchange coefficient  $H_{sf}$  is assumed to be constant  
<sup>267</sup> for the sake of simplicity. Then the energy exchange can be written as:

$$q_{sf} = H_{sf}(T_f - T_s) \quad (23)$$

<sup>268</sup> On the other hand, the drag force can be calculated as:

$$f_d = K(\mathbf{U}_s - \mathbf{U}_f) \quad (24)$$

269 For the momentum exchange between fluid flows and porous media, we as-  
 270 sume that the drag force  $\mathbf{f}_d$  depends on the average grain size of the grains  
 271  $D_p$ , the porosity  $n$ , the fluid viscosity  $\mu_f$ , and is proportional to the relative  
 272 velocities of soil grains and fluid  $(\mathbf{U}_s - \mathbf{U}_f)$ . Based on recent investigation  
 273 of CFD simulations of fluid flow around mono- and bi-disperse packing of  
 274 spheres for  $0.1 < \phi_s < 0.6$  and  $Re < 1000$  [28]. The drag force is given by:  
 275

$$\mathbf{f}_d = \frac{18\phi_s(1-\phi_s)\mu_f}{D_p^2} F(\phi_s, Re)(\mathbf{U}_s - \mathbf{U}_f) \quad (25)$$

276 where Reynolds number  $Re$  are computed as:

$$Re = \frac{n\rho_f D_p}{\mu_f} \|\mathbf{U}_s - \mathbf{U}_f\| \quad (26)$$

277 The function  $F(\phi_s, Re)$  can be calculated as:

$$F(\phi_s, Re) = F(\phi_s, 0) + \frac{0.413Re}{24(1-\phi_s)^2} \left( \frac{(1-\phi_s)^{-1} + 3\phi_s(1-\phi_s) + 8.4Re^{-0.343}}{1 + 10^{3\phi_s} Re^{-(1+4\phi_s)/2}} \right) \quad (27)$$

278 where the low Reynold coefficient  $F(\phi_s, Re \rightarrow 0)$  is:

$$F(\phi_s, 0) = \frac{10\phi_s}{(1-\phi_s)^2} + (1-\phi_s)^2(1 + 1.5\sqrt{\phi_s}) \quad (28)$$

279 When validating the model with analytical solution, it requires to know the  
 280 hydraulic conductivity  $K$ . In such case, we convert the equation (25) to  
 281 Kozeny-Carman formula by assuming  $F(\phi_s, Re) = 10\phi_s/(1-\phi_s)^2$ , leading to

$$\mathbf{f}_d = \frac{180\phi_s^2\mu_f}{D_p^2(1-\phi_s)} (\mathbf{U}_s - \mathbf{U}_f) \quad (29)$$

282 Then, the draging force following the Darcy law is given by:

$$\mathbf{f}_d = \frac{n^2\mu_f}{\kappa} (\mathbf{U}_s - \mathbf{U}_f) \quad (30)$$

283 where  $\kappa$  being intrinsic permeability of soil which can be written as:

$$\kappa = \frac{K\mu_f}{\rho_f g} \quad (31)$$

284 As such, the hydraulic conductivity will be expressed as:

$$K = \frac{D_p^2(1-\phi_s)^3}{180\phi_s^2\mu_f} \rho_f g \quad (32)$$

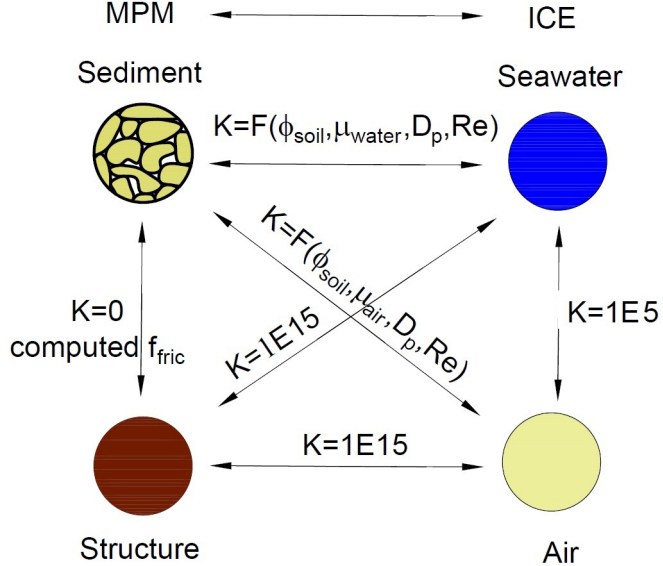


Figure 3: Momentum exchange coefficient between materials

285 Solving momentum and energy exchange with an implicit solver

286 The derivation of the implicit integration for the momentum exchange is  
 287 presented in the Appendix's section 'Momentum and energy exchange with  
 288 an implicit solver'. The linear equations for multi phases  $i,j=1:N$  has the  
 289 form as:

$$\begin{vmatrix} (1 + \beta_{ij}) & -\beta_{ij} \\ -\beta_{ji} & (1 + \beta_{ji}) \end{vmatrix} \begin{vmatrix} \Delta \mathbf{U}_i \\ \Delta \mathbf{U}_j \end{vmatrix} = \begin{vmatrix} \beta_{ij} (\mathbf{U}_i^* - \mathbf{U}_j^*) \\ \beta_{ji} (\mathbf{U}_i^* - \mathbf{U}_j^*) \end{vmatrix}$$

290 where the intermediate velocity for fluid phases  $f=1:N_f$  and for solid/porous  
 291 phases  $s=1:N_s$  can be calculated by:

$$\begin{aligned} \mathbf{U}_f^* &= \mathbf{U}_f^n + \Delta t \left( -\frac{\nabla P_f^{n+1}}{\rho_f^n} + \frac{\nabla \cdot \boldsymbol{\tau}_f^n}{\bar{\rho}_f^n} + \mathbf{b} \right) \\ \mathbf{U}_s^* &= \mathbf{U}_s^n + \Delta t \left( \frac{\nabla \cdot \boldsymbol{\sigma}'^n}{\bar{\rho}_s^n} - \frac{\nabla P_f^{n+1}}{\rho_s} + \mathbf{b} \right) \end{aligned} \quad (33)$$

292 Also, the momentum exchange coefficient can be computed at every time  
 293 step as  $\beta_{12} = K/\bar{\rho}_f^n$  and  $\beta_{21} = K/\bar{\rho}_s^n$  with the coefficient depending on the  
 294 different type of interactions (see Figure 3) as for example:

295

- 296 1. The drag force is set to zero in soil-structure interactions, and instead  
 297 the frictional force is computed.  
 298 2. As a result of fluid-structure interaction, the momentum exchange coef-  
 299 ficient should be extremely high (1E15) when the solid material points  
 300 are considered to be zero-porosity/zero-permeability.  
 301 3. In the case of soil-fluid interaction, the drag force is calculated using  
 302 the equation (25). Considering that air has a much lower viscosity than  
 303 water, its drag force is much lower than the drag force of water in a  
 304 pore.  
 305 4. A momentum exchange coefficient of 1E5 is applied between multiphase  
 306 flows. This value is far higher than reality [29], but it is necessary to  
 307 have enough numerical stability to conduct simulations in the numerical  
 308 example.

309 Similar approach applied for the energy exchange term leading to:

$$\begin{vmatrix} (1 + \eta_{ij}) & -\eta_{ij} \\ -\eta_{ji} & (1 + \eta_{ji}) \end{vmatrix} \begin{vmatrix} \Delta T_i \\ \Delta T_j \end{vmatrix} = \begin{vmatrix} \eta_{ij}(T_i^n - T_j^n) \\ \eta_{ji}(T_j^n - T_i^n) \end{vmatrix}$$

310 with  $\eta$  being the energy exchange coefficient.

311 *Equation of state for fluid phases*

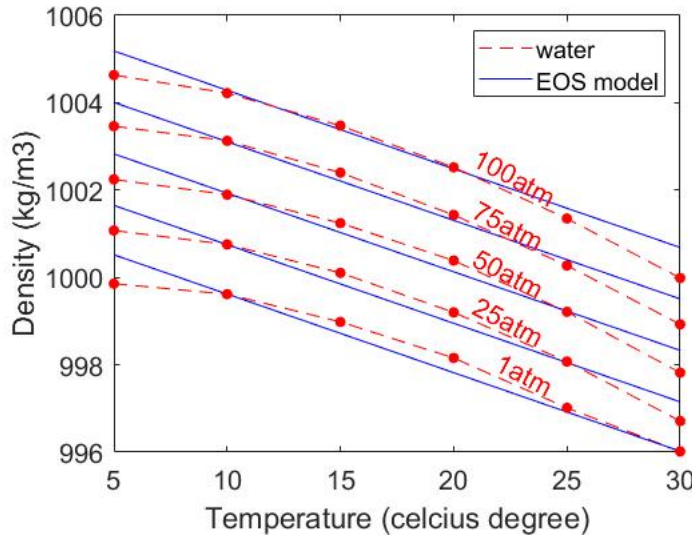


Figure 4: Equation of state of water

312     The equation of state establishes relations between thermodynamics vari-  
 313     ables  $[P_f, \rho_f, T_f]$ . The choice of the equation of state depends on the types  
 314     of the fluid materials. For example, for the air, it is possible to assume the  
 315     equation of state for the perfect gas which obeys:

$$P_f = \rho_f R T_f \quad (34)$$

316     where  $R$  is the gas constant. For the water, a simple linear equation of state  
 317     is in the following form:

$$P_f = P_{ref} + K_f(\rho_f - \rho_{ref} + \alpha_f(T_f - T_{ref})) \quad (35)$$

318     where reference pressure  $P_{ref} = 1 \text{ atm} = 101325 \text{ Pa}$ , reference temperature  
 319      $T_{ref} = 10^\circ\text{C}$ , reference density  $\rho_{ref} = 999.8 \text{ kg/m}^3$ , the bulk modulus of water  
 320      $K_f = 2 \text{ GPa}$ , and the water thermal expansion  $\alpha_f = 0.18 \text{ }^\circ\text{C}^{-1}$ . Equation  
 321     (35) matches well with the state of the water (see Figure 4).

322     **Numerical implementation**

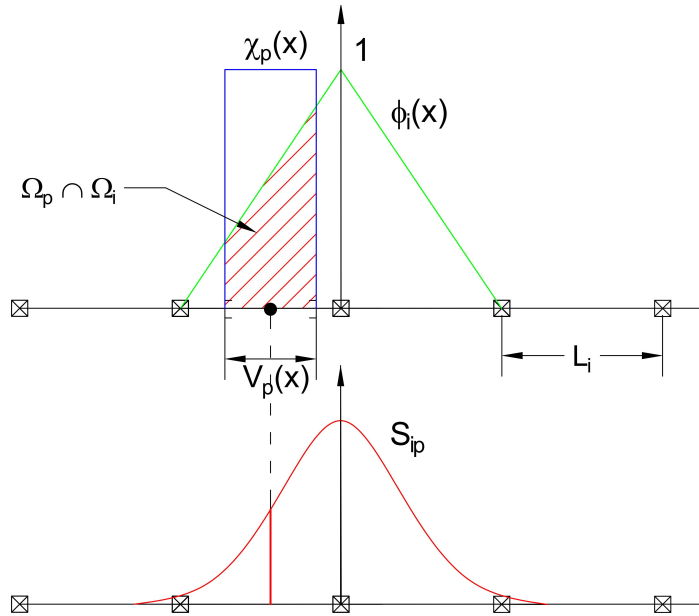


*Figure 5: GIMP weighting function (red as a convolution of the linear basis shape function (green) and the characteristic function (blue))*

323 The fluid phases are discretized in the grid with the state variables stored  
 324 at the centroid of the cells  $[\rho_{f,c}, \mathbf{U}_{f,c}, T_{f,c}, v_{f,c}]$  while the solid phase is dis-  
 325 cretized in the particles with the state variables  $[m_{sp}, \mathbf{U}_{sp}, T_{sp}, \boldsymbol{\sigma}'_{sp}]$ . In the  
 326 Material Point Method, we use the generalized interpolation technique [30]  
 327 using the weight function as a convolution of a grid shape function  $N_i(\mathbf{x})$  in  
 328 a nodal domain  $\Omega_i$  and a characteristic function  $\chi_p(\mathbf{x})$  in a particle domain  
 329  $\Omega_p$  with the volume  $V_p(\mathbf{x})$  as follows:

$$S_{ip} = \frac{1}{V_p} \int_{\Omega_i \cap \Omega_p} N_i(\mathbf{x}) \chi_p(\mathbf{x}) d\mathbf{x} \quad (36)$$

330 where the volume  $V_p(\mathbf{x})$  of the material point p can be calculated as:

$$V_p = \int_{\Omega_p} \chi_p(\mathbf{x}) d\mathbf{x} \quad (37)$$

331 The characteristic function is the Heaviside function as  $\chi_p = 1$  if  $\mathbf{x} \in \Omega_p$ ,  
 332 otherwise 0 (see Figure 5). For the interpolation of the centroid of the cell,  
 333 the linear basis function is used as:

$$S_{ci} = N_i(\mathbf{x}_c) \quad (38)$$

334 The time discretization are solved using the following steps.

335 *Interpolation from Solid Particle to Grid*

336 The nodal values of the solid state (mass, velocity, temperature, volume)  
 337 are:

$$\begin{aligned} m_{si}^n &= \sum S_{ip} m_{sp} \\ \mathbf{U}_{si}^n &= \frac{\sum S_{ip} (m\mathbf{U})_{sp}^n}{m_{si}^n} \\ T_{si}^n &= \frac{\sum S_{ip} (mT)_{sp}^n}{m_{si}^n} \\ V_{si}^n &= \frac{\sum S_{ip} (mV)_{sp}^n}{m_{si}^n} \\ \boldsymbol{\sigma}_{si}^n &= \frac{\sum S_{ip} (\boldsymbol{\sigma}V)_{sp}^n}{V_{si}^n} \end{aligned} \quad (39)$$

338 The nodal internal forces is calculated by:

$$\mathbf{f}_{si}^{int,n} = - \sum \nabla S_{ip} (\boldsymbol{\sigma}'_{sp})^n V_{sp}^n \quad (40)$$

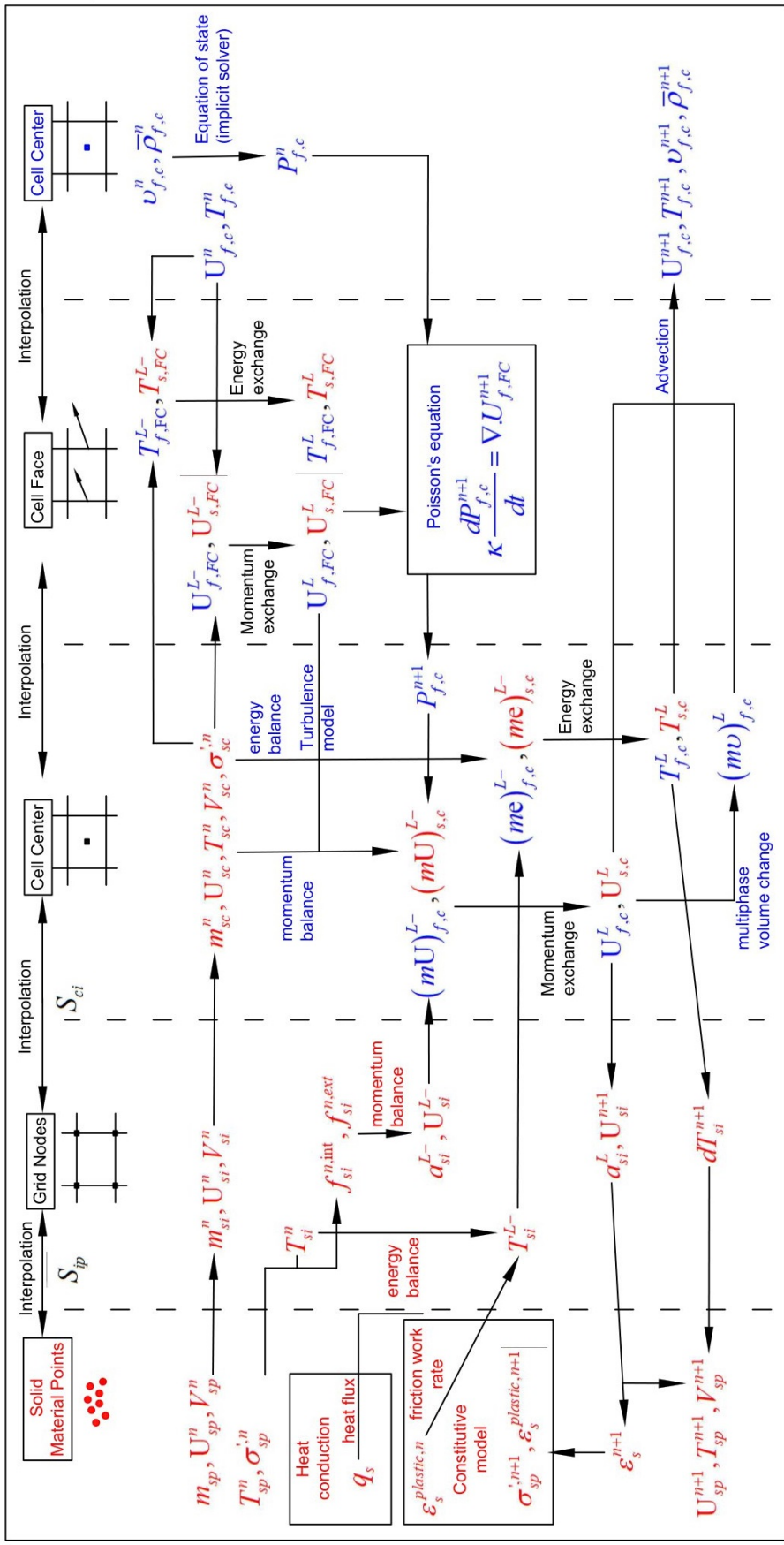


Figure 6: Numerical implementation of MPMICE

339 The nodal external forces  $f_{si}^{ext,n}$  and the frictional forces from soil-structure  
 340 interaction  $f_{fric,si}^n$  from contact between materials are computed here.  
 341 Then we compute the solid cell variables as:

$$\begin{aligned} m_{sc}^n &= \sum S_{ci} m_{si} \\ \rho_{sc}^n &= \frac{m_{sc}^n}{V} \\ \mathbf{U}_{sc}^n &= \sum S_{ci} \mathbf{U}_{si}^n \\ T_{sc}^n &= \sum S_{ci} T_{si}^n \\ V_{sc}^n &= \sum S_{ci} V_{si}^n \\ \boldsymbol{\sigma}_{sc}^n &= \sum S_{ci} \boldsymbol{\sigma}_{si}^n \end{aligned} \tag{41}$$

342 *Compute equation of state for fluid phase*

343 The total fluid material volume of a cell is:

$$V_{total} = \sum_{f=1}^{N_f} M_f v_f \tag{42}$$

344 We need to find  $P_{f,c}^n$  which allows each fluid materials obey their equation of  
 345 states  $[P_f, \rho_f, v_f, T_f, e_f]$  but also allow mass of all fluid materials to fill the  
 346 entire the pore volume without ongoing compression or expansion following  
 347 the condition as follows:

$$0 = n - \sum_{f=1}^{N_f} v_f \bar{\rho}_f \tag{43}$$

348 Then, we can use the Newton-Raphson interation to find the value of  $P_{f,c}^n$   
 349 which satisfies the equation (42, 43) and each equation of states of each fluid  
 350 materials.

351 *Compute cell face velocity*

352 Following the derivation in the Appendix: Advanced Fluid Pressure, we  
 353 first compute the fluid cell face velocity as:

$$\mathbf{U}_{f,FC}^{L-} = \frac{(\bar{\rho} \mathbf{U})_{f,FC}^n}{\bar{\rho}_{f,FC}^n} + \Delta t \left( -\frac{\nabla^{FC} P_{f,c}^n}{\rho_{f,FC}^n} + \frac{\nabla^{FC} \cdot \boldsymbol{\tau}^n}{\bar{\rho}_{s,FC}} + \mathbf{b} \right) \tag{44}$$

354 The equation (44) is discretized in three dimension (noted that  $\nabla^{FC} \cdot \boldsymbol{\tau} = 0$ ),  
 355 for example the discretized equation in the x direction is:

$$U_{fx}^{L-} = \frac{(\bar{\rho}U)_{fx,R}^n + (\bar{\rho}U)_{fx,L}^n}{\bar{\rho}_{fx,L}^n + \bar{\rho}_{fx,R}^n} + \Delta t \left( -\frac{2(v_{fx,L}^n v_{fx,R}^n)}{v_{fx,L}^n + v_{fx,R}^n} \frac{P_{f,cx,R}^n - P_{f,cx,L}^n}{\Delta x} + b_x \right) \quad (45)$$

356 The cell face solid velocity can be calculated as:

$$\mathbf{U}_{s,FC}^{L-} = \frac{(\bar{\rho}\mathbf{U})_{s,FC}^n}{\bar{\rho}_{s,FC}^n} + \Delta t \left( \frac{\nabla^{FC} \cdot \boldsymbol{\sigma}_c'^n}{\bar{\rho}_{s,FC}} - \frac{\nabla^{FC} P_{f,c}^n}{\rho_s} + \mathbf{b} \right) \quad (46)$$

357 The equation (46) is discretized in three dimension (noted that  $\nabla^{FC} \cdot \boldsymbol{\sigma}_{ij} = 0$   
 358 with  $i \neq j$ ), for example the discretized equation in the x direction is:

$$U_{sx}^{L-} = \frac{(\bar{\rho}U)_{sx,R}^n + (\bar{\rho}U)_{sx,L}^n}{\bar{\rho}_{sx,L}^n + \bar{\rho}_{sx,R}^n} + \Delta t \left( \frac{2(\sigma_{xx,R} - \sigma_{xx,L})}{(\bar{\rho}_{sx,L}^n + \bar{\rho}_{sx,R}^n) \Delta x} - \frac{P_{f,cx,R}^n - P_{f,cx,L}^n}{\rho_s \Delta x} + b_x \right) \quad (47)$$

359 Then, we compute the modified cell face velocity  $\mathbf{U}_{FC}^L$  considering the mo-  
 360 mentum exchange (see the Appendix: Momentum exchange with an implicit  
 361 solve) as follows:

$$\begin{aligned} \mathbf{U}_{f,FC}^L &= \mathbf{U}_{f,FC}^{L-} + \Delta \mathbf{U}_{f,FC} \\ \mathbf{U}_{s,FC}^L &= \mathbf{U}_{s,FC}^{L-} + \Delta \mathbf{U}_{s,FC} \end{aligned} \quad (48)$$

362 The linear equation below is solved to obtain the increment of velocity with  
 363  $i,j = 1 : N$  as:

$$\begin{vmatrix} (1 + \beta_{ij}) & -\beta_{ij} \\ -\beta_{ji} & (1 + \beta_{ji}) \end{vmatrix} \begin{vmatrix} \Delta \mathbf{U}_{i,FC} \\ \Delta \mathbf{U}_{j,FC} \end{vmatrix} = \begin{vmatrix} \beta_{ij} (\mathbf{U}_{i,FC}^{L-} - \mathbf{U}_{j,FC}^{L-}) \\ \beta_{ji} (\mathbf{U}_{j,FC}^{L-} - \mathbf{U}_{i,FC}^{L-}) \end{vmatrix}$$

#### 364 Compute cell face temperature

365 Similar to the velocity, the faced temperature is computed, for example  
 366 in x direction, as:

$$\begin{aligned} T_{fx}^{L-} &= \frac{(\bar{\rho}T)_{fx,R}^n + (\bar{\rho}T)_{fx,L}^n}{\bar{\rho}_{fx,L}^n + \bar{\rho}_{fx,R}^n} \\ T_{sx}^{L-} &= \frac{(\bar{\rho}T)_{sx,R}^n + (\bar{\rho}T)_{sx,L}^n}{\bar{\rho}_{sx,L}^n + \bar{\rho}_{sx,R}^n} \end{aligned} \quad (49)$$

367 Then, we compute the modified cell face temperature  $T_{FC}^L$  considering the  
 368 energy exchange (see the Appendix: Momentum and energy exchange with

<sup>369</sup> an implicit solver) as follows:

$$\begin{aligned} T_{f,FC}^L &= T_{f,FC}^{L-} + \Delta T_{f,FC} \\ T_{s,FC}^L &= T_{s,FC}^{L-} + \Delta T_{s,FC} \end{aligned} \quad (50)$$

<sup>370</sup> The linear equation below is solved to determine the increment of tempera-  
<sup>371</sup> ture due to energy exchange with  $i,j = 1 : N$  as:

$$\begin{vmatrix} (1 + \eta_{ij}) & -\eta_{ij} \\ -\eta_{ji} & (1 + \eta_{ji}) \end{vmatrix} \begin{vmatrix} \Delta T_{i,FC} \\ \Delta T_{j,FC} \end{vmatrix} = \begin{vmatrix} \eta_{ij}(T_{i,FC}^{L-} - T_{j,FC}^{L-}) \\ \eta_{ji}(T_{j,FC}^{L-} - T_{i,FC}^{L-}) \end{vmatrix}$$

<sup>372</sup> *Compute fluid pressure (implicit scheme)*

<sup>373</sup> For single phase flow, the increment of the fluid pressure can be computed  
<sup>374</sup> as:

$$\kappa_f \frac{\Delta P}{dt} = \nabla^c \cdot \mathbf{U}_{f,FC}^{n+1} \quad (51)$$

<sup>375</sup> For multi-phase flows, the increment of the fluid pressure of the mixture can  
<sup>376</sup> be computed as:

$$\kappa \frac{\Delta P}{dt} = \sum_{f=1}^{N_f} \nabla^c \cdot (\phi_{f,FC} \mathbf{U}_{f,FC})^{n+1} \quad (52)$$

<sup>377</sup> where  $\kappa = \sum_{f=1}^{N_f} (\phi_{f,FC} \kappa_f) / \sum_{f=1}^{N_f} (\phi_{f,FC})$ . Then, the fluid pressure at cell  
<sup>378</sup> center is:

$$P_c^{n+1} = P_c^n + \Delta P_c^n \quad (53)$$

<sup>379</sup> Finally, the cell face advanced fluid pressure is:

$$P_{FC}^{n+1} = \left( \frac{P_{c,L}^{n+1}}{\bar{\rho}_{f,L}^n} + \frac{P_{c,R}^{n+1}}{\bar{\rho}_{f,R}^n} \right) / \left( \frac{1}{\bar{\rho}_{f,L}^n} + \frac{1}{\bar{\rho}_{f,R}^n} \right) = \left( \frac{P_{c,L}^{n+1} \bar{\rho}_{f,R}^n + P_{c,R}^{n+1} \bar{\rho}_{f,L}^n}{\bar{\rho}_{f,L}^n \bar{\rho}_{f,R}^n} \right) \quad (54)$$

<sup>380</sup> *Compute viscous shear stress term of the fluid phase*

<sup>381</sup> This part compute the viscous shear stress  $\Delta(m\mathbf{U})_{f,c,\tau}$  for a single vis-  
<sup>382</sup> cous compressible Newtonian fluid and optionally shear stress induced by the  
<sup>383</sup> turbulent model.

384    ***Compute nodal internal temperature of the solid phase***

385    The nodal internal temperature rate is computed based on the heat con-  
 386    duction model as below:

$$dT_{si}^{L-} = \frac{(\Delta W_{si}^n + \Delta W_{fric,i}^n + \nabla^i \cdot \mathbf{q}_{si}^n)}{m_{si}^n c_v} \quad (55)$$

387    where  $\Delta W_{si}^n = \boldsymbol{\sigma}' : \frac{D_s(\boldsymbol{\epsilon}_s^p)}{Dt}$  is the mechanical work rate computed from the  
 388    constitutive model with  $\boldsymbol{\epsilon}_s^p$  is the plastic strain,  $\Delta W_{fric,i}^n$  is the work rate  
 389    computed from the contact law due to the frictional sliding between solid  
 390    materials. The heat flux is  $\mathbf{q}_s = \bar{\rho}_s \beta_s \nabla T_s$  with  $\beta_s$  being the thermal conduc-  
 391    tivity of the solid materials.

$$T_{si}^{L-} = T_{si}^n + dT_{si}^{L-} \quad (56)$$

392    ***Compute and integrate acceleration of the solid phase***

393    After interpolating from material points to the nodes, the nodal acceler-  
 394    ation and velocity are calculated by:

$$\mathbf{a}_{si}^{L-} = \frac{\mathbf{f}_{si}^{int,n} + \mathbf{f}_{si}^{ext,n}}{m_{si}^n} + \mathbf{g} \quad (57)$$

$$\mathbf{U}_{si}^{L-} = \mathbf{U}_{si}^n + \mathbf{a}_{si}^{L-} \Delta t \quad (58)$$

396    ***Compute Lagrangian value (mass, momentum and energy)***

397    For the fluid phase, the linear momentum rate, the energy rate are:

$$\Delta(m\mathbf{U})_{f,c} = V n_c^n \nabla^c P_c^{n+1} + \Delta(m\mathbf{U})_{f,c,\tau} + V \bar{\rho}_{f,c}^n g \quad (59)$$

$$\Delta(me)_{f,c} = V n_c^n P_c^{n+1} \nabla^c \cdot \mathbf{U}_{f,FC}^* + \nabla^c \cdot \mathbf{q}_{f,c}^n \quad (60)$$

399    The heat flux is  $\mathbf{q}_f = \bar{\rho}_f \beta_f \nabla T_f$  with  $\beta_f$  being the thermal conductivity of the  
 400    fluid materials. The Lagrangian value of the mass, linear momentum and  
 401    energy of fluid phases without momentum exchange are:

$$m_{f,c}^L = V \bar{\rho}_{f,c}^n \quad (61)$$

$$(m\mathbf{U})_{f,c}^{L-} = V \bar{\rho}_{f,c}^n \mathbf{U}_{f,c}^n + \Delta(m\mathbf{U})_{f,c} \quad (62)$$

$$(me)_{f,c}^{L-} = V \bar{\rho}_{f,c}^n T_{f,c}^n c_v + \Delta(me)_{f,c} \quad (63)$$

404 For the solid phase, the Lagrangian value of the linear momentum and energy  
 405 of solid phase are:

$$m_{sc}^L = m_{sc}^n \quad (64)$$

$$(m\mathbf{U})_{sc}^{L-} = \sum S_{ci} m_{si}^n \mathbf{U}_{si}^{L-} + V(1 - n_c^n) \nabla^c P_{f,c}^{n+1} \quad (65)$$

$$(me)_{sc}^{L-} = \sum S_{ci} m_{si}^n T_{si}^L c_v \quad (66)$$

408 To consider the momentum exchange, the Lagrangian velocity is modified as:

$$\begin{aligned} \mathbf{U}_{f,c}^L &= \mathbf{U}_{f,c}^{L-} + \Delta \mathbf{U}_{f,c} \\ \mathbf{U}_{sc}^L &= \mathbf{U}_{sc}^{L-} + \Delta \mathbf{U}_{sc} \end{aligned} \quad (67)$$

409 where the cell-centered intermediate velocity can be calculated by:

$$\begin{aligned} \mathbf{U}_{f,c}^{L-} &= \frac{(m\mathbf{U})_{f,c}^{L-}}{m_{f,c}^L} \\ \mathbf{U}_{sc}^{L-} &= \frac{(m\mathbf{U})_{sc}^{L-}}{m_{sc}^L} \end{aligned} \quad (68)$$

410 And the increment of the velocity  $\mathbf{U}_{f,c}$ ,  $\Delta \mathbf{U}_{sc}$  can be computed by solving  
 411 the linear equation with  $i,j = 1:N$  as:

$$\begin{vmatrix} (1 + \beta_{ij}) & -\beta_{ij} \\ -\beta_{ji} & (1 + \beta_{ji}) \end{vmatrix} \begin{vmatrix} \Delta \mathbf{U}_{i,c} \\ \Delta \mathbf{U}_{j,c} \end{vmatrix} = \begin{vmatrix} \beta_{ij} (\mathbf{U}_{i,c}^{L-} - \mathbf{U}_{j,c}^{L-}) \\ \beta_{ji} (\mathbf{U}_{j,c}^{L-} - \mathbf{U}_{i,c}^{L-}) \end{vmatrix}$$

412 To consider the energy exchange, the Lagrangian temperature is modified as:

$$\begin{aligned} T_{f,c}^L &= T_{f,c}^{L-} + \Delta T_{f,c} \\ T_{sc}^L &= T_{sc}^{L-} + \Delta T_{sc} \end{aligned} \quad (69)$$

413 where the cell-centered intermediate temperature can be calculated by:

$$\begin{aligned} T_{f,c}^{L-} &= \frac{(mT)_{f,c}^{L-}}{m_{f,c}^L c_v} \\ T_{sc}^{L-} &= \frac{(mT)_{sc}^{L-}}{m_{sc}^L c_v} \end{aligned} \quad (70)$$

414 And the increment of the temperature due to energy exchange can be com-  
 415 puted by solving the linear equation with  $i,j = 1:N$  as:

$$\begin{vmatrix} (1 + \eta_{ij}) & -\eta_{ij} \\ -\eta_{ji} & (1 + \eta_{ji}) \end{vmatrix} \begin{vmatrix} \Delta T_{i,c} \\ \Delta T_{j,c} \end{vmatrix} = \begin{vmatrix} \eta_{ij} (T_{i,c}^{L-} - T_{j,c}^{L-}) \\ \eta_{ji} (T_{j,c}^{L-} - T_{i,c}^{L-}) \end{vmatrix}$$

<sup>416</sup> Finally, we obtain the cell-centered solid acceleration and temperature rate  
<sup>417</sup> as:

$$d\mathbf{U}_{sc}^L = \frac{(m\mathbf{U})_{sc}^L - (m\mathbf{U})_{sc}^n}{m_{sc}^L \Delta t} \quad (71)$$

$$dT_{sc}^L = \frac{(me)_{sc}^L - (me)_{sc}^n}{m_{sc}^L c_v \Delta t} \quad (72)$$

#### <sup>419</sup> Compute Lagrangian specific volume of the fluid phase

<sup>420</sup> To compute the Lagrangian value of the specific volume of the fluid phase,  
<sup>421</sup> we need to compute the Lagrangian temperature rate as below:

$$T_{f,c}^{n+1} = \frac{(me)_{f,c}^L}{m_{f,c}^L c_v} \quad (73)$$

$$\frac{D_f T_{f,c}}{Dt} = \frac{T_{f,c}^{n+1} - T_{f,c}^n}{\Delta t} \quad (74)$$

<sup>423</sup> As such, the Lagrangian specific volume rate is:

$$\Delta(mv)_{f,c} = V f_{f,c}^\phi \nabla \cdot \mathbf{U} + (\phi_{f,c} \alpha_{f,c} \frac{D_f T_{f,c}}{Dt} - f_{f,c}^\phi \sum_{n=1}^N \phi_{nc} \alpha_{nc} \frac{D_n T_{n,c}}{Dt}) \quad (75)$$

<sup>424</sup> where  $f_f^\phi = (\phi_f \kappa_f) / (\sum_{n=1}^N \phi_n \kappa_n)$  and  $\mathbf{U} = \nabla \cdot (\sum_{s=1}^{N_s} \phi_{sc} \mathbf{U}_{sc} + \sum_{f=1}^{N_f} \phi_{fc} \mathbf{U}_{f,c})$ .  
<sup>425</sup> Finally, the Lagrangian specific volume is:

$$(mv)_{f,c}^L = V \bar{\rho}_{f,c}^n v_{f,c}^n + \Delta(mv)_{f,c} \quad (76)$$

#### <sup>426</sup> Compute advection term and advance in time

<sup>427</sup> The mass, linear momentum, energy and specific volume with advection  
<sup>428</sup> are:

$$m_{f,c}^{n+1} = m_{f,c}^L - \Delta t \nabla \cdot (\bar{\rho}_{f,c}^L, \mathbf{U}_{f,FC}^L) \quad (77)$$

$$(m\mathbf{U})_{f,c}^{n+1} = (m\mathbf{U})_{f,c}^L - \Delta t \nabla \cdot ((\bar{\rho}\mathbf{U})_{f,c}^L, \mathbf{U}_{f,FC}^L) \quad (78)$$

$$(me)_{f,c}^{n+1} = (me)_{f,c}^L - \Delta t \nabla \cdot ((\bar{\rho}c_v T)_{f,c}^L, \mathbf{U}_{f,FC}^L) \quad (79)$$

$$(mv)_{f,c}^{n+1} = (mv)_{f,c}^L - \Delta t \nabla \cdot ((\bar{\rho}v)_{f,c}^L, \mathbf{U}_{f,FC}^L) \quad (80)$$

<sup>432</sup> Finally, the state variables of the fluid phases of the next time step are:

$$\bar{\rho}_{f,c}^{n+1} = \frac{m_{f,c}^{n+1}}{V} \quad (81)$$

433

$$\mathbf{U}_{f,c}^{n+1} = \frac{(m\mathbf{U})_{f,c}^{n+1}}{m_{f,c}^{n+1}} \quad (82)$$

434

$$T_{f,c}^{n+1} = \frac{(me)_{f,c}^{n+1}}{m_{f,c}^{n+1}} \quad (83)$$

435

$$v_{f,c}^{n+1} = \frac{(mv)_{f,c}^{n+1}}{m_{f,c}^{n+1}} \quad (84)$$

436 *Interpolate from cell to node of the solid phase*

437 First we interpolate the acceleration, velocity and temperature rate to  
438 the node as below:

$$\mathbf{a}_{si}^n = \sum S_{ci} d\mathbf{U}_{sc}^L \quad (85)$$

439

$$\mathbf{U}_{si}^{n+1} = \sum S_{ci} d\mathbf{U}_{sc}^L \Delta t \quad (86)$$

440

$$dT_{si}^n = \sum S_{ci} dT_{sc}^L \quad (87)$$

441 Then the boundary condition and contact forces  $f_{si}^{fric}$  are applied to the nodal  
442 velocity, and then accelerations are modified by:

$$\mathbf{a}_{si}^n = \frac{\mathbf{v}_{si}^{n+1} - \mathbf{v}_{si}^n}{\Delta t} \quad (88)$$

443 *Update the particle variables*

444 The state variables of the solid phase  $[\mathbf{U}_{sp}^{n+1}, \mathbf{x}_{sp}^{n+1}, \nabla \mathbf{U}_{sp}^{n+1}, T_{sp}^{n+1}, \nabla T_{sp}^{n+1}, \mathbf{F}_{sp}^{n+1}, V_{sp}^{n+1}]$   
445 (velocity, position, velocity gradient, temperature, temperature gradient, de-  
446 formation gradient, volume) are updated as:

$$\mathbf{U}_{sp}^{n+1} = \mathbf{U}_{sp}^n + \sum S_{sp} \mathbf{a}_{si}^n \Delta t \quad (89)$$

447

$$\mathbf{x}_{sp}^{n+1} = \mathbf{x}_{sp}^n + \sum S_{sp} \mathbf{U}_{si}^{n+1} \Delta t \quad (90)$$

448

$$\nabla \mathbf{U}_{sp}^{n+1} = \sum \nabla S_{sp} \mathbf{U}_{si}^{n+1} \quad (91)$$

449

$$T_{sp}^{n+1} = T_{sp}^n + \sum S_{sp} dT_{si}^n \Delta t \quad (92)$$

450

$$\nabla T_{sp}^{n+1} = \sum \nabla S_{sp} T_{sp}^n \Delta t \quad (93)$$

$$\mathbf{F}_{sp}^{n+1} = (\mathbf{I} + \nabla \mathbf{U}_{sp}^{n+1} \Delta t) \mathbf{F}_{sp}^n \quad (94)$$

$$V_{sp}^{n+1} = \det(\mathbf{F}_{sp}^{n+1}) V_{sp}^o \quad (95)$$

Finally, the effective stress ( $\sigma'$ )<sup>n+1</sup> is updated from the constitutive model and the pore water pressure is interpolated from the cell as:

$$p_f^{n+1} = \sum S_{si} P_c^{n+1} \quad (96)$$

455 Numerical validation

For all simulations, water is characterized by a bulk modulus of 2 GPa, a density of 998 kg/m<sup>3</sup> at a reference temperature of 5 degrees Celsius and a reference pressure of 10325 Pa (1 atm), and a dynamic viscosity denoted as  $\mu_f$  of 1 mPa s. The air is treated as an ideal gas with a density of 1.17 kg/m<sup>3</sup> at a reference temperature of 5 degrees Celsius and a reference pressure of 10325 Pa (1 atm), and it possesses a dynamic viscosity  $\mu_f$  of  $18.45 \times 10^{-3}$  mPa s.”

463 *Fluid Flow through isothermal porous media*

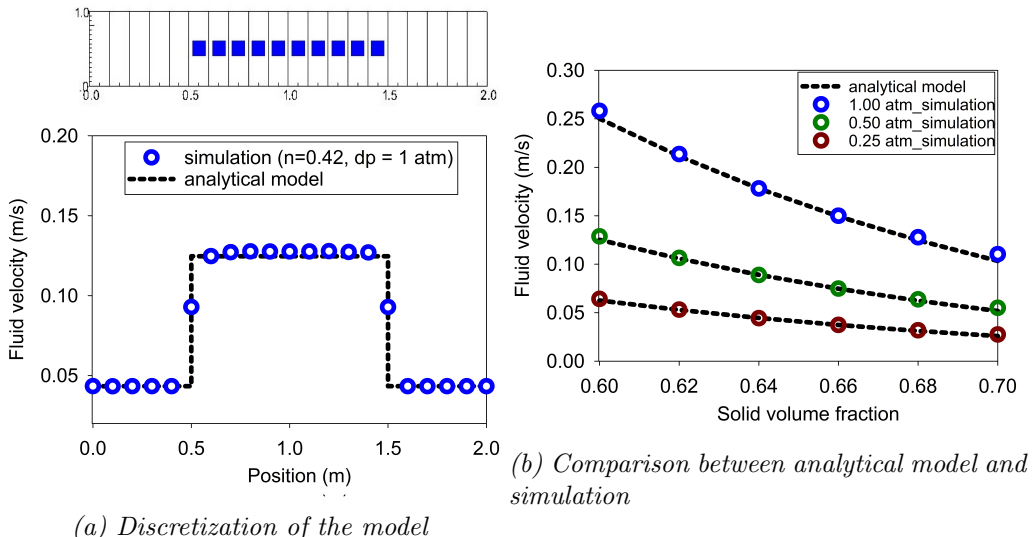


Figure 7: Numerical results of the fluid flow through isothermal porous media

464 Fluid flow through porous media is important in many engineering disciplines,  
 465 like predicting water flow in soil. Fluid flow velocity in one dimension  
 466 can be calculated from the porous media's hydraulic conductivity  $K$  as:

$$467 \quad U_f = K \frac{\Delta p_f}{L} \quad (97)$$

468 If the Carman-Kozeny formula is adopted  $F = 10\phi_s/(1 - \phi_s)^2$ , the hydraulic  
 469 conductivity will be expressed as  $K = D_p^2(1 - \phi_s)^3\rho_f g/180\phi_s^2\mu_f$ . Then, the  
 470 analytical formula of average velocity in one dimension through the porous  
 471 media is:

$$472 \quad U_f = \frac{1}{n} \frac{D_p^2(1 - \phi_s)^3}{180\phi_s^2\mu_f} \frac{\Delta p_f}{L} \quad (98)$$

473 Our numerical model's validity is confirmed through the simulation of  
 474 fluid flow in a 1m long porous medium. This porous medium is represented  
 475 by an elastic material with the following properties: Young's modulus of  
 476 10 MPa, Poisson's ratio of 0.3, and a density of 2650 kg/m<sup>3</sup>. The volume  
 477 fraction of the porous medium, denoted as  $\phi_s$ , is varied as [0.6, 0.62, 0.66,  
 478 0.68, 0.7], while the average grain diameter  $d$  is set at 1mm. The model is  
 479 discretized into 20 finite elements, with the porous medium represented by  
 480 10 finite elements, each containing one material point per element. We apply  
 481 pressure gradients with three different values: [0.25, 0.5, 1] atm. As depicted  
 482 in Figure 7, our model demonstrates excellent agreement with theoretical  
 483 predictions in simulating fluid flow.

#### 484 *Isothermal consolidation*

485 A common benchmark for fully saturated porous media is the simulation  
 486 of one-dimensional consolidation. Using the Carman-Kozeny formula, the  
 487 time-dependent pressure can be calculated as:

$$488 \quad p_f = \sum_{m=1}^{\infty} \frac{2F_{ext}}{M} \sin\left(\frac{Mz}{H}\right) e^{-M^2 T_V} \text{ with } M = \frac{\pi}{2}(2m + 1) \quad (99)$$

489 Here, the consolidation rate is defined as  $T_v = C_v t / H^2$ , the consolidation  
 490 coefficient as  $C_v = E_v n^3 d^2 / (180(1 - n)^2 \mu)$ , and the Oedometer modulus as  
 $E_v = E(1 - v) / (1 + v) / (1 - 2v)$ .

491 To validate our numerical model, we simulated the consolidation of a  
 492 1m column of porous media. The porous media is modeled as an elastic

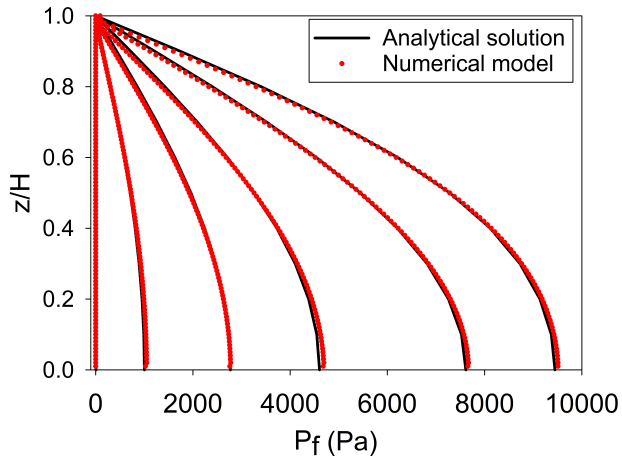


*Figure 8: Comparison between analytical solution and numerical solution*

material with a Young's modulus of 10 MPa, a Poisson's ratio of 0.3, and a density of  $2650 \text{ kg/m}^3$ . The volume fraction of porous media  $\phi_s$  is set to 0.7, equivalent to a porosity of 0.3, and the average grain diameter  $d$  is 1 mm. The model is discretized into 100 finite elements, each with 1 material point per element. An external pressure of 10 kPa is applied to the top of the column. Figure 8 demonstrates a strong agreement between the predicted fluid flow and theoretical results.

#### 500 *Thermal induced cavity flow*

Another benchmark involves the study of thermally-induced cavity flow in porous media. This simulation calculates temperature and velocity distributions within a square, non-deformable, saturated porous medium. The top and bottom walls are insulated, while the left and right walls maintain a fixed temperature gradient of 1 degree, leading to fluid motion in the form of cavity flow due to temperature-induced density variation. Our numerical model is validated by comparing it with the numerical solution obtained using the finite element method.

The porous medium in this simulation is modeled as a non-deformable material with a density of  $2500 \text{ kg/m}^3$ . The specific heat capacity of the water and porous skeleton is  $4181 \text{ J/kg}\cdot\text{K}$  and  $835 \text{ J/kg}\cdot\text{K}$ , respectively. Thermal conductivity values are  $0.598 \text{ W/m}\cdot\text{K}$  for water and  $0.4 \text{ W/m}\cdot\text{K}$  for the porous skeleton. The volume fraction of porous media  $\phi_s$  is set at 0.6, equivalent

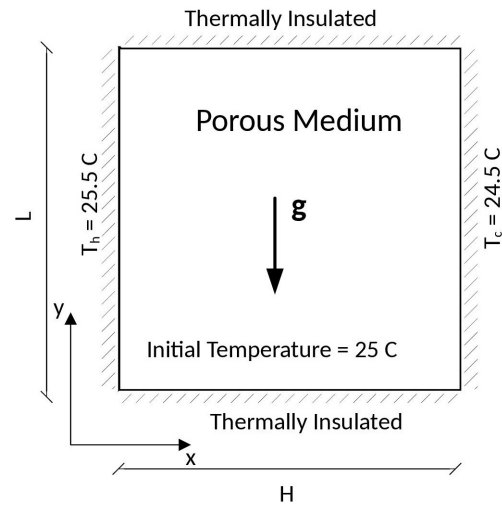


Figure 9: Model schematic [31]

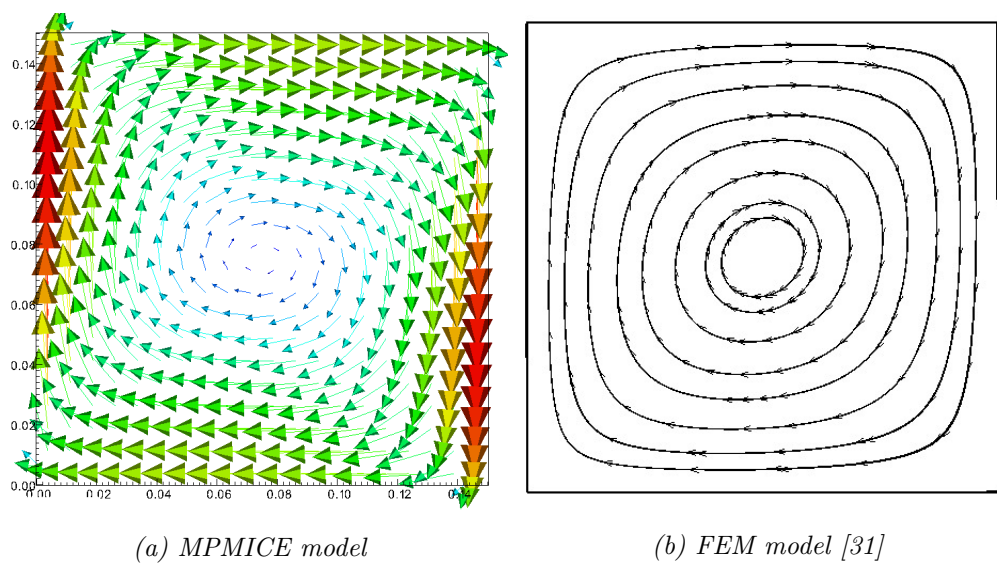


Figure 10: Comparison between MPMICE model and FEM model

514 to a porosity of 0.4, and the average grain diameter  $d$  is 1mm. The model  
 515 is discretized into a 20x20 grid of finite elements, with 4 material points per  
 516 element. Figure 10 demonstrates that our numerical results align well with  
 517 the numerical solution obtained using the finite element method.

518 **Numerical examples**

519 *Underwater debris flow*

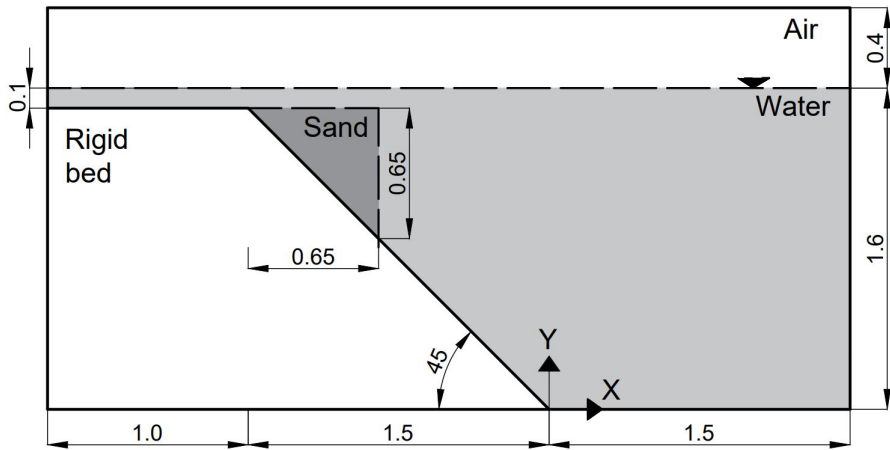


Figure 11: Model schematic

520 The numerical example is compared to the experimental work of Rzad-  
 521 kiewicz et al. on submarine debris flow [32]. In their experiment, sand within  
 522 a triangular box is released and slides along a rigid bed inclined at 45 de-  
 523 grees underwater (see Figure 11). The material properties in the numerical  
 524 model are chosen based on Rzadkiewicz et al.'s experiment [32]. The sand  
 525 has a saturated density of  $1985 \text{ kg/m}^3$  and a friction angle of 10 degrees.  
 526 Young's modulus, despite its negligible effect on debris flow run-out due to  
 527 extreme deformation, is set at 50 MPa with a Poisson's ratio of 0.25. The  
 528 rigid bed, significantly stiffer, possesses bulk modulus and shear modulus  
 529 values of  $117E^7 \text{ Pa}$  and  $43.8E^7 \text{ Pa}$ , respectively. The numerical parameters  
 530 used in this example are outlined in Table 1.  
 531 The boundary conditions applied in the numerical model are as follows: all  
 532 boundary faces have zero velocity ( $U = 0 \text{ m/s}$ ) and a temperature of 5 degrees  
 533 Celsius ( $T = 5^\circ\text{C}$ ). At the top boundary, pressure has a Neumann boundary

534 condition of  $dp/dx = 0$  kPa, and density has a Neumann boundary condition  
 535 of  $d\rho/dx = 0$   $kg/m^3$ . The background mesh comprises 700 x 400 cells,  
 536 resulting in a total of 280,000 cells. Each cell within the debris flow and rigid  
 537 bed contains 2 x 2 material points.

538 Figure 12b illustrates snapshots of underwater debris flow sliding, effectively  
 539 capturing the typical hydroplaning mechanism of the debris flow. Hydroplaning  
 540 refers to the lifting of the debris flow, causing it to lose contact with the  
 541 bottom layer. In addition, Figure 13 compares the elevation of the free  
 542 surface at 0.4s and 0.8s between our proposed method and other methods,  
 543 demonstrating the alignment of our computed results with experimental re-  
 544 sults [7].

545 What sets our model apart is its utilization of effective stress analysis in-  
 546 stead of total stress analysis. This allows for the analysis of water pressure  
 547 and temperature within the debris flow. Furthermore, we investigate the dif-  
 548 ferences between underwater debris flow and saturated debris flow in terms  
 549 of their interaction with obstacles. Figure 12 presents snapshots of simula-  
 550 tions of both underwater and saturated debris flow. The saturated debris  
 551 flow (Figure 12a) exhibits behavior similar to frictional flow, with grains in  
 552 contact with each other. Conversely, underwater debris flow (Figure 12b)  
 553 behaves like turbulent flow, with grains separated and showing no contact  
 554 forces, as reflected by the near-zero effective stress in the turbulence domain.

Materials	Bulk modul (Pa)	Shear modul (Pa)	Density (kg/m3)	Temp (C)	Dynamic viscosity (Pa s)	Friction angle (degrees)
Water (at surface)	2.15e9	-	999.8	5	855e-6	-
Air (at top boundary)	-	-	1.177	5	18.45e-6	-
Sand (porous media)	8.33e6	20e6	1985	5	-	10
Rigid bed (solid)	117e7	43.8e7	8900	5	-	-

Table 1: Numerical parameters for the underwater submarine debris flow

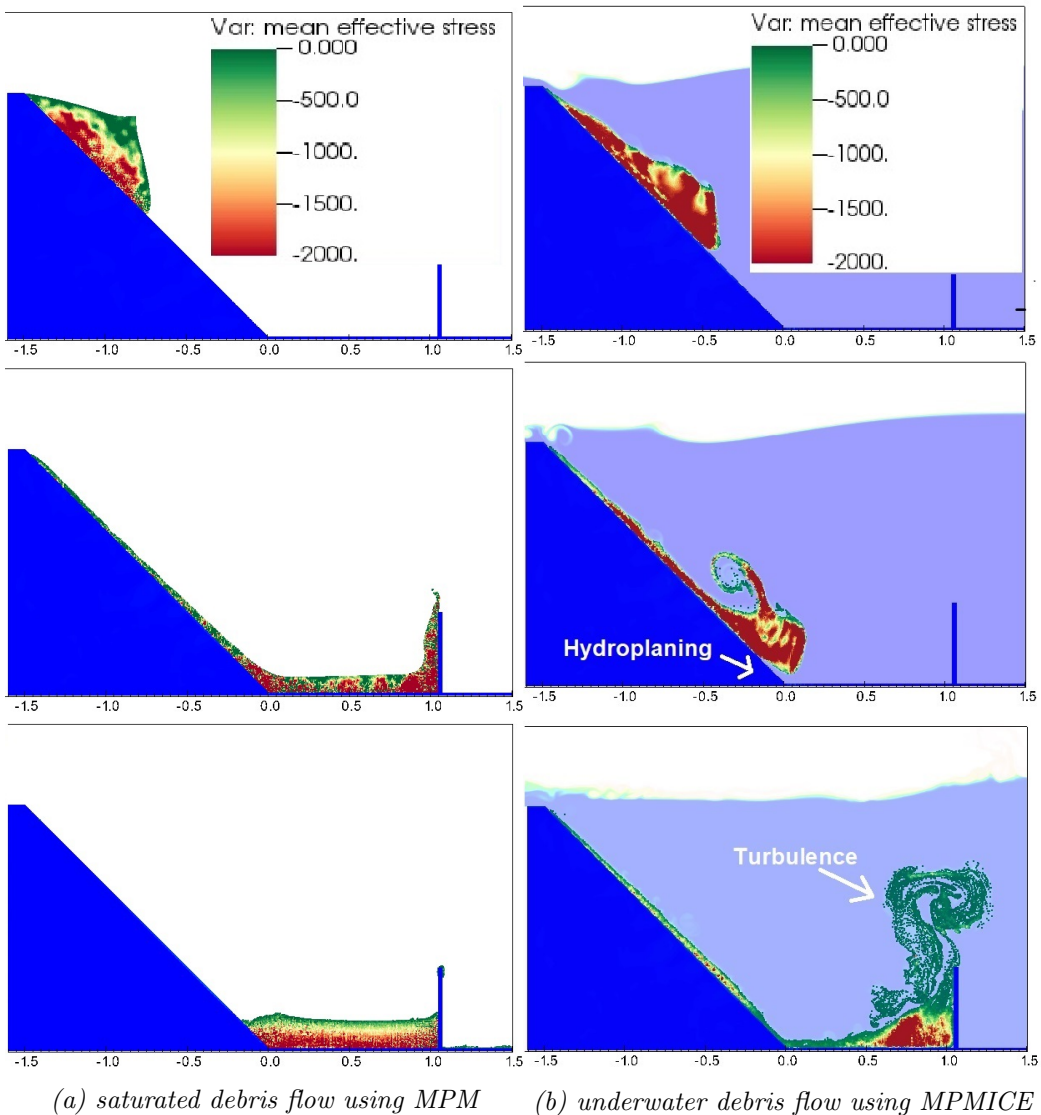
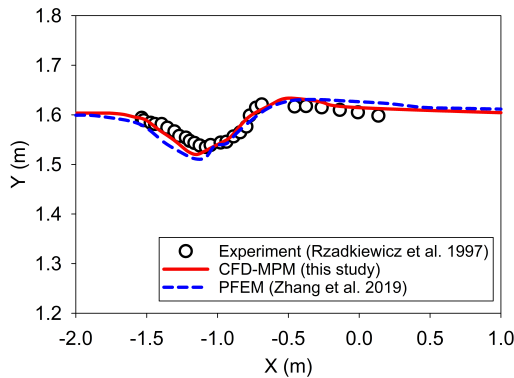
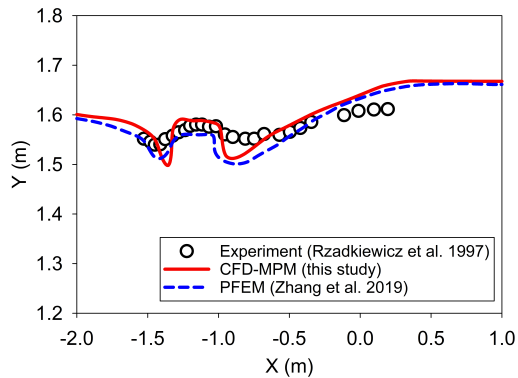


*Figure 12: Simulation of Debris Flow: Mean Effective Stress Distribution (Green Color Indicates Near-Zero Effective Stress)*



(a) 0.4 seconds



(b) 0.8 seconds

*Figure 13: Evolution of water level in the simulation of underwater debris flow*

555 Validation of soil response to the seismic loading

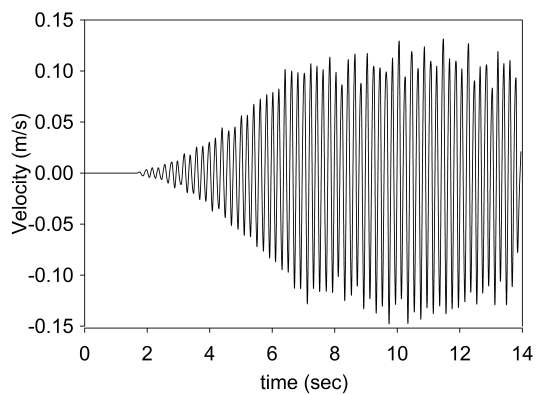


*Figure 14: Seismic loading*

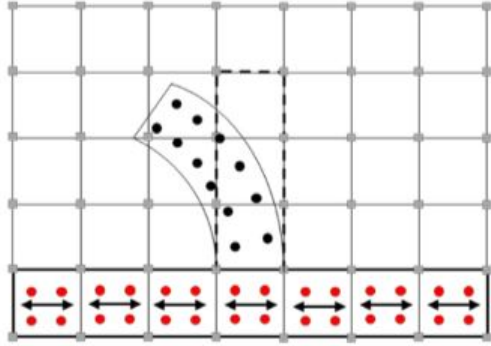


Figure 15: Material points prescribed velocity as kinematic boundary condition [33]

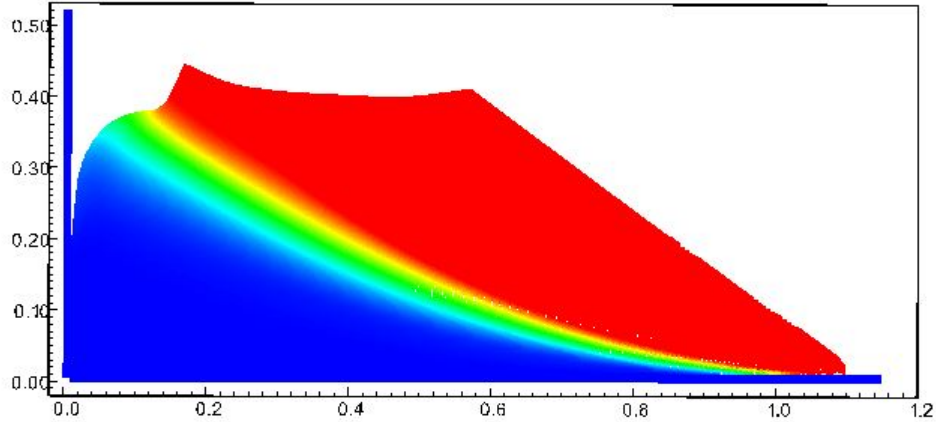


Figure 16: Numerical model of the seismic-induced slope failure with displacement color

556 An experimental study conducted by Hiraoka et al. [34] aimed to invest-  
 557igate the influence of seismic shaking on the deformation of a 0.5 m-high  
 558 sand slope. The sand used in the experiment was partially saturated, with a  
 559 moisture content of 10 percent. The provided soil parameters for the Mohr  
 560 Coulomb model include the effective friction angle of 23 degrees, apparent  
 561 cohesion of 0.78 kPa, Young's modulus of 2.57 MPa, Poisson's ratio of 0.33,  
 562 and moist unit weight of 16.5 kN/m<sup>3</sup>. The soil's dilatancy angle was assumed  
 563 to be 0 [34]. The experimental setup consisted of a shaking table box with a  
 564 steel horizontal base and smooth glass vertical sidewalls. Laser sensors were  
 565 used to monitor the displacement of the slope's toe and crest. Figure 14

566 displays the velocity-time history employed in the experiment.  
 567 To simulate the seismic loading in our numerical model, we adopted a method  
 568 presented by Alsardi et al. [33], which involves specifying the velocity at the  
 569 corresponding material points representing either the shaking table or the  
 570 bedrock at the site (see Figure 15). In our simulation, we considered the  
 571 horizontal base to be fully rough and the vertical contact to be fully smooth.  
 572 The initial stress condition was initiated using gravity, and seismic loading  
 573 induced the slope failure (see Figure 16).  
 574 Previous studies by Bhandari et al. [35], Alsardi et al. [33], and Hiraoka  
 575 et al. [34] attempted to model this experiment using MPM and SPH mod-  
 576 els. In this study, we compared our results with those obtained from other  
 577 particle-based methods (Figure 17). The main difference is that we did not  
 578 apply 5 percent numerical damping in our model, unlike the other methods.  
 579 We found that the final displacement of the slope toe in our MPM model was  
 580 higher than that observed in the experiment. Nevertheless, the validation of  
 581 the Mohr-Coulomb model under seismic response demonstrated reasonable  
 582 soil behavior in terms of displacement.

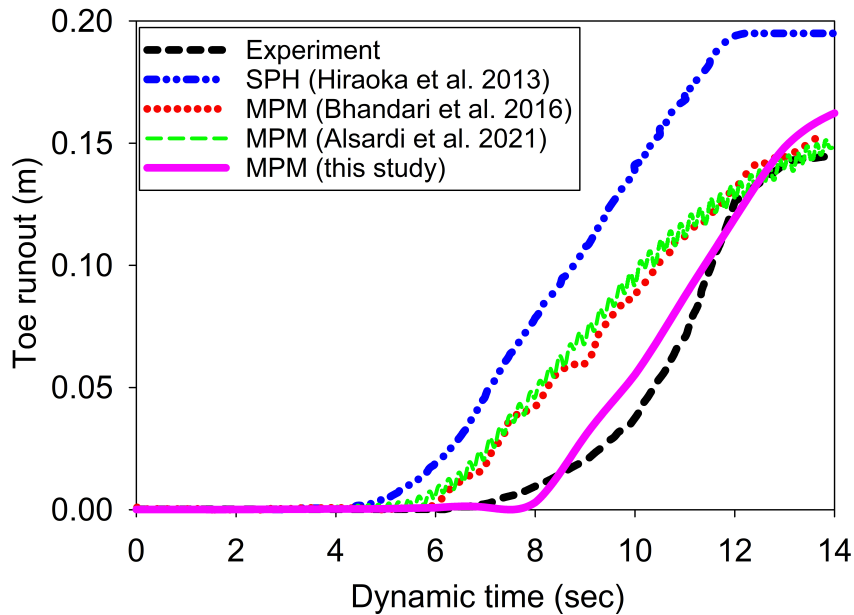


Figure 17: Displacement of the toe of the slope

583 *Earthquake-induced submarine landslides*

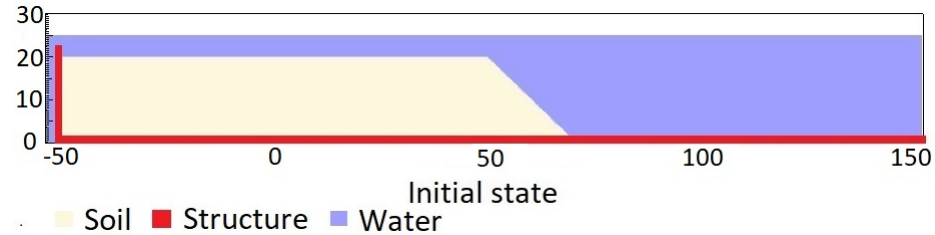


Figure 18: Numerical simulation of the earthquake-induced submarine landslide

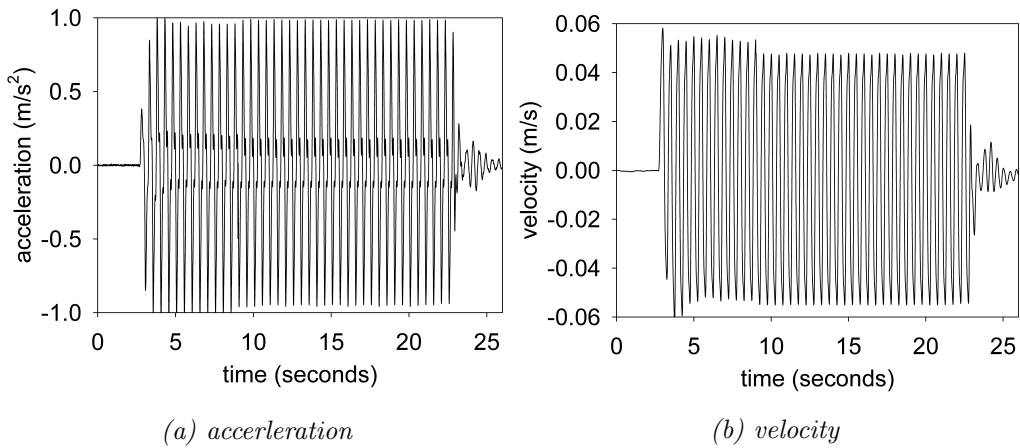


Figure 19: Ground acceleration profile, frequency of 2Hz and magnitude of 1g

584 In the final example, we conduct a numerical analysis of earthquake-  
 585 induced submarine landslides. We utilize a plane strain model featuring an  
 586 underwater slope, as depicted in Figure 18. This model consists of a 20m high  
 587 slope with a gradient of 45 degrees, placed within a horizontal and vertical  
 588 structure formerly used as a shaking table to apply earthquake loading. To  
 589 simplify the earthquake loading, we simulate ground shaking for 20 seconds,  
 590 maintaining a constant ground acceleration of 1g and a consistent frequency  
 591 of 2 Hz (Figure 19a). This magnitude of earthquake is plausible; for instance,  
 592 during the 2023 Turkey-Syria Earthquake, significant ground shaking with  
 593 peak ground acceleration exceeding 1g was recorded at numerous locations.  
 594 This real-world example demonstrates the practical occurrence of such high  
 595 levels of ground acceleration during seismic events. To generate the seismic

596 loading, we employ the same method as presented in the previous numerical  
 597 example.

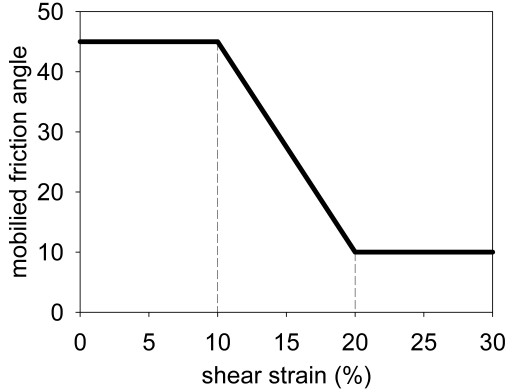


Figure 20: Mobilized friction angle in Mohr Coulomb model

598 A non-associated Mohr-Coulomb model is employed to represent the soil  
 599 in our simulation. The soil grains have a density of  $2650 \text{ kg/m}^3$ , a Young's  
 600 modulus of 10 kPa, a Poisson's ratio of 0.3, and zero cohesion. The mobilized  
 601 friction angle  $\phi'_m$  is determined based on the softening curve (as depicted in  
 602 Figure 20), with a peak friction angle  $\phi'_p$  of 45 degrees and a residual friction  
 603 angle  $\phi'_r$  of 10 degrees. The porosity is set to 0.3, and the average grain  
 604 size of the soil is approximately  $0.1 \mu\text{m}$  to mimic undrained behavior. The  
 605 mobilized dilatancy angle is calculated using Rowe's stress dilatancy theory  
 606 [36] as follows:

$$\sin \psi'm = \frac{\sin \phi'm - \sin \phi'r}{1 - (\sin \phi'r \sin \phi'_m)} \quad (100)$$

607 The solid plane is modeled as a rigid body, acting as a shaking table. Frictional  
 608 contact with a friction coefficient of 0.1 is considered between the  
 609 horizontal plane and the sand. No artificial damping is applied in the sim-  
 610 ulation. The contact between the vertical plane and the sand is treated as  
 611 smooth, with a zero friction coefficient.

612 Symmetric boundary conditions are imposed on all boundary faces, while  
 613 Neumann boundary conditions are applied at the top boundary for pressure  
 614 ( $d\rho/dx = 0 \text{ kPa}$ ) and density ( $d\rho/dx = 0 \text{ kg/m}^3$ ). In the context of the  
 615 simulation, a symmetric boundary condition means that the normal compo-  
 616 nent of the velocity at the boundary face is set to zero, and the tangential

617 component matches the tangential component of the neighboring cells.  
 618 The mesh size is set to 0.25 m x 0.25 m, resulting in 300,852 element cells  
 619 and 142,316 material points. The simulation takes several hours to complete  
 620 60 seconds of simulation time, utilizing 4,096 CPUs.

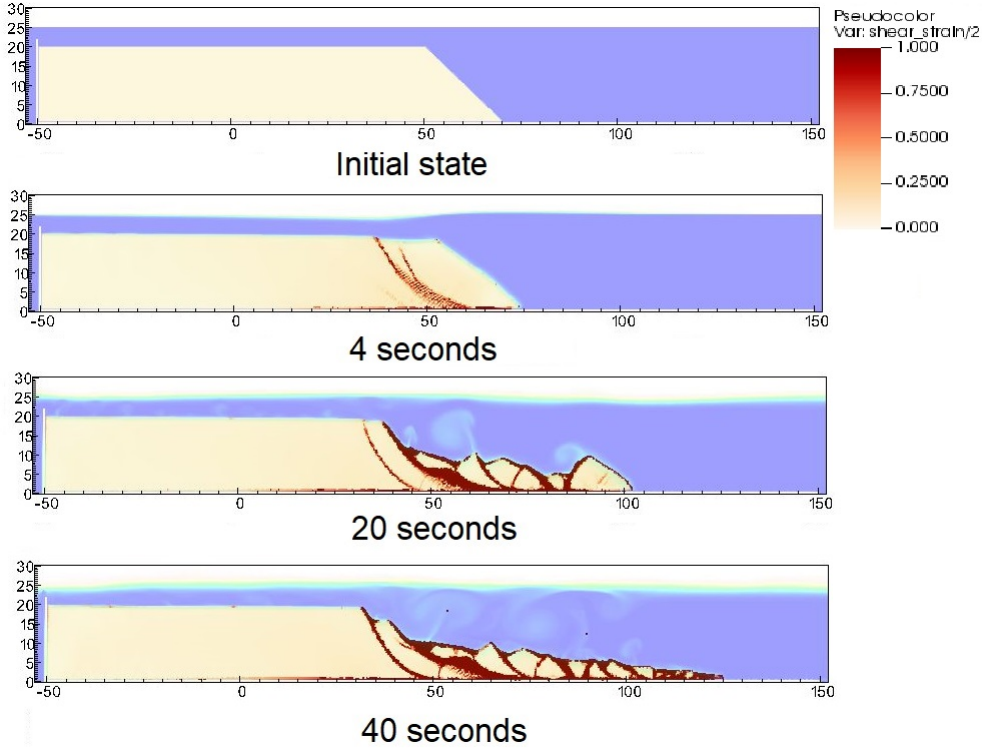


*Figure 21: Shear strain during the earthquake-induced submarine landslides*

621 We have illustrated the entire process and mechanism of earthquake-  
 622 induced submarine landslides by presenting the shear strain (Figure 21),  
 623 pore water pressure in atm (Figure 22), and velocity (Figure 23). The failure  
 624 mechanism can be characterized as a progressive failure mechanism, and here  
 625 are some key numerical observations:

- 626 1. At the onset of the seismic event, the seismic loading triggers the initial  
 627 slide at 3 seconds. By 4 seconds, the debris starts moving at a maximum  
 628 speed of around 2-3 m/s, with multiple shear bands developing in the  
 629 slope. A wave is generated from the submarine slide, propagating with  
 630 approximately 2-3 m high in the direction of the slide.

- 631     2. When the onset of the shear band occurs in the slope (e.g., at 4 seconds  
 632       and 20 seconds), negative excess pore water pressure develops along  
 633       this shear band, with pore water pressure dropping below 1 atm. This  
 634       behavior is typical of dilatancy when the soil undergoes rapid shearing  
 635       in an undrained state.  
 636     3. As the seismic loading ends at 23 seconds, the last shear band is mobi-  
 637       lized, and the slope quickly reaches its final deposition. There are no  
 638       further progressive failures in the slope at this stage. A turbulent flow  
 639       develops due to the interaction between the debris flow and seawater.  
 640     In summary, we have presented a comprehensive view of the earthquake-  
 641       induced submarine landslides, covering (1) the earthquake-triggering mech-  
 642       anism, (2) the initiation of shear bands with the development of negative  
 643       excess pore water pressure, (3) the progressive failure mechanism, and (4)  
 644       the generation of submarine landslide-induced waves leading to the final de-  
 645       position of debris.

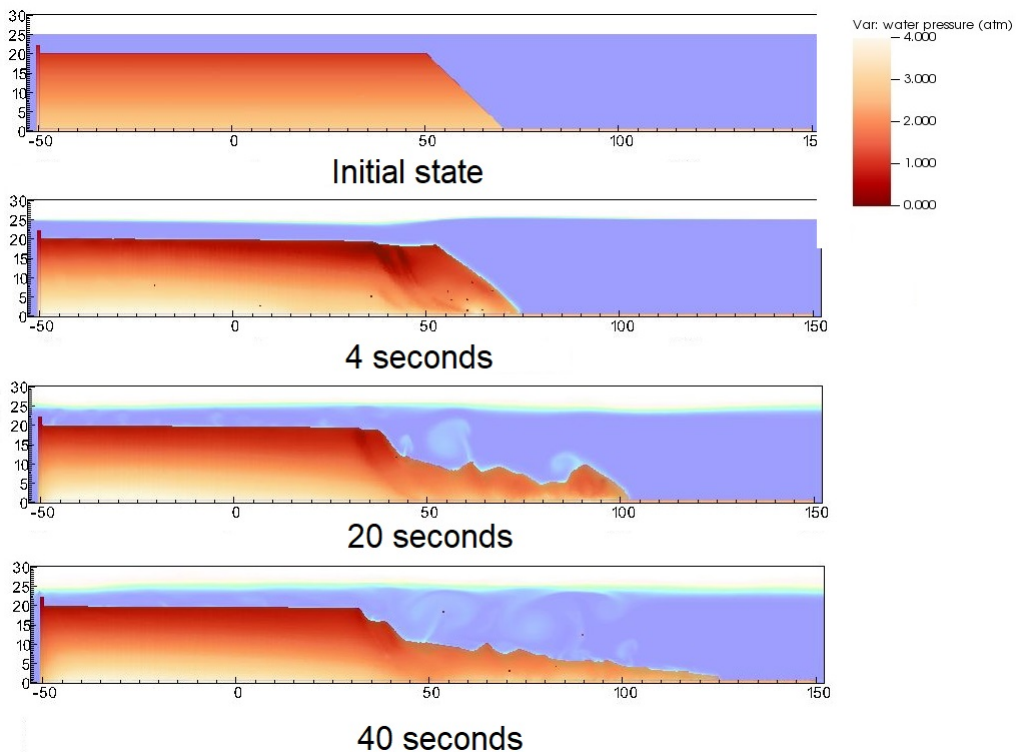


*Figure 22: pore water pressure during the earthquake-induced submarine landslides*

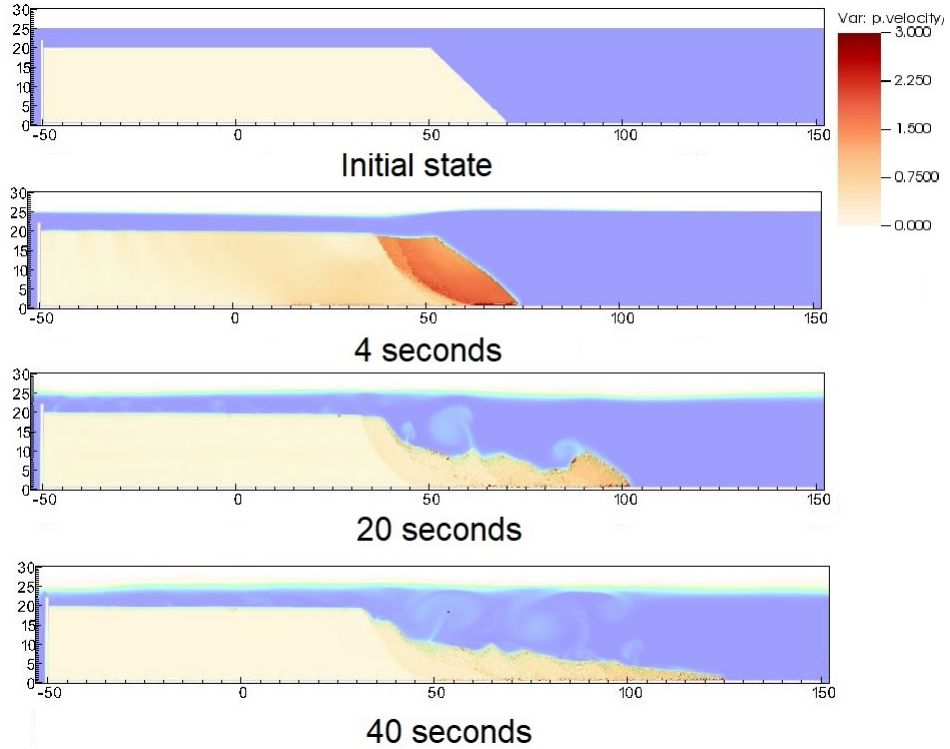


*Figure 23: Velocity during the earthquake-induced submarine landslides*

## 646      **Conclusions**

647      We have introduced a numerical approach called MPMICE for simulating  
 648      large deformation soil-fluid-structure interactions, with a specific focus  
 649      on earthquake-induced submarine landslides. This model leverages two key  
 650      components: Material Point Method (MPM): MPM is employed to accu-  
 651      rately capture the large deformations occurring in iso-thermal porous me-  
 652      dia and solid structures. Implicit Continuous Eulerian (CFD Formulation):  
 653      This component is used for modeling the intricate fluid flow, including tur-  
 654      bulence, within the system. It adopts a compressible, conservative multi-  
 655      material CFD formulation. Our model has been implemented within the  
 656      high-performance Uintah computational framework and rigorously validated  
 657      through comparisons with analytical solutions and experimental data. Sub-  
 658      sequently, we have demonstrated the model's capabilities in simulating the  
 659      complete process of earthquake-induced submarine landslides.

660 **Acknowledgements**

661 The authors gratefully acknowledge Dr. James Guilkey and Dr. Todd  
662 Harman from the University of Utah for sharing the insight on the theoretical  
663 framework of MPMICE which this work is based. This project has received  
664 funding from the European Union’s Horizon 2020 research and innovation  
665 program under the Marie Skłodowska-Curie Actions (MSCA) Individual Fel-  
666 lowship (Project SUBSLIDE “Submarine landslides and their impacts on  
667 offshore infrastructures”) grant agreement 101022007. The authors would  
668 also like to acknowledge the support from the Research Council of Norway  
669 through its Centers of Excellence funding scheme, project number 262644  
670 Porelab. The computations were performed on High Performance Comput-  
671 ing resources provided by UNINETT Sigma2 - the National Infrastructure  
672 for High Performance Computing and Data Storage in Norway.

673 **Data Availability Statement**

674 The authors confirm that the data supporting the findings of this study  
675 are available within the article. All input files and the analytical calculations  
676 in this section are provided in the Github repository  
677 ([https://github.com/QuocAnh90/Uintah\\_NTNU](https://github.com/QuocAnh90/Uintah_NTNU)) for the reproduction of the  
678 numerical results.

679 **Appendix: Equation derivation**

680 Before deriving the governing equation, we define the Lagrangian deriva-  
681 tive for a state variable  $f$  as:

$$\frac{D_f f}{Dt} = \frac{\partial f}{\partial t} + \mathbf{U}_f \cdot \nabla f \quad (101)$$

$$\frac{D_s f}{Dt} = \frac{\partial f}{\partial t} + \mathbf{U}_s \cdot \nabla f \quad (102)$$

683 We adopt the following definitions as per [22]:

$$-\frac{1}{V} \left[ \frac{\partial V_f}{\partial p} \right] \equiv \kappa_f \quad \text{isothermal compressibility of fluid} \quad (103)$$

$$\frac{1}{V} \left[ \frac{\partial V_f}{\partial T} \right] \equiv \alpha_f \quad \text{constant pressure thermal expansivity of fluid} \quad (104)$$

685 Then, we calculate the rate of volume within incompressible solid grains as  
 686 follows:

$$\frac{1}{V} \frac{D_f V_f}{Dt} = \frac{1}{V} \left( \left[ \frac{\partial V_f}{\partial p} \right] \frac{D_f P_{eq}}{Dt} + \left[ \frac{\partial V_f}{\partial T_f} \right] \frac{D_f T}{Dt} \right) = \frac{1}{V} \left( -\kappa_f \frac{D_f P_{eq}}{Dt} + \alpha_f \frac{D_f T_f}{Dt} \right) \quad (105)$$

687 *Evolution of porosity*

688 Solving the solid mass balance equation (4) with the definition of solid  
 689 mass in equation (2), we obtain the rate of porosity as:

$$\frac{D_s m_s}{Dt} = \frac{D_s (\phi_s \rho_s V)}{Dt} = \rho_s V \frac{D_s \phi_s}{Dt} + \phi_s V \frac{D_s \rho_s}{Dt} + \phi_s \rho_s \frac{D_s V}{Dt} = 0 \quad (106)$$

690 Since soil grains are assumed to be incompressible, term 2 on the right-hand  
 691 side is zero, resulting in:

$$V \frac{D_s \phi_s}{Dt} + \phi_s \frac{D_s V}{Dt} = 0 \quad (107)$$

692 Dividing all terms by "V" and using the equation  $\frac{1}{V} \frac{D_s V}{Dt} = \nabla \cdot \mathbf{U}_s$ , we get:

$$\frac{D_s n}{Dt} = \frac{\partial n}{\partial t} + \mathbf{U}_s \cdot \nabla n = \phi_s \nabla \cdot \mathbf{U}_s \quad (108)$$

693 *Momentum conservation*

694 The linear momentum balance equations for the fluid phases based on  
 695 mixture theory are given by:

$$\frac{1}{V} \frac{D_f (m_f \mathbf{U}_f)}{Dt} = \nabla \cdot (-\phi_f p_f \mathbf{I}) + \nabla \cdot \boldsymbol{\tau}_f + \bar{\rho}_f \mathbf{b} + \sum \mathbf{f}_d + \mathbf{f}_b \quad (109)$$

697 On the right hand side, the terms include the divergence of partial fluid phase  
 698 stress, body force, drag force (momentum exchange) and buoyant force as  
 699 described in [37] for immiscible mixtures, which takes the form:

$$\mathbf{f}_b = \boldsymbol{\sigma}_f \nabla(n) \quad (110)$$

700 Hence, the linear momentum balance equations for the fluid phases become:

$$\frac{1}{V} \frac{D_f (m_f \mathbf{U}_f)}{Dt} = -\phi_f \nabla p_f + \nabla \cdot \boldsymbol{\tau}_f + \bar{\rho}_f \mathbf{b} + \sum \mathbf{f}_d \quad (111)$$

701 The Reynolds stress component can be included in the term  $\boldsymbol{\tau}_f$  to consider the  
 702 turbulent effects if needed. To derive the linear momentum balance equation  
 703 for the solid phase, we begin with the linear momentum balance equation for  
 704 the mixture as:

$$\frac{1}{V} \frac{D_f(m_f \mathbf{U}_f)}{Dt} + \frac{1}{V} \frac{D_s(m_s \mathbf{U}_s)}{Dt} = \nabla \cdot (\boldsymbol{\sigma}) + \bar{\rho}_f \mathbf{b} + \bar{\rho}_s \mathbf{b} \quad (112)$$

705 Combining Terzaghi's equation (3) and subtracting both sides with equation  
 706 (111), we obtain the linear momentum balance equations for the solid phase  
 707 as:

$$\frac{1}{V} \frac{D_s(m_s \mathbf{U}_s)}{Dt} = \nabla \cdot (\boldsymbol{\sigma}') - \phi_s \nabla p_f + \bar{\rho}_s \mathbf{b} - \sum \mathbf{f}_d + \sum \mathbf{f}_{fric} \quad (113)$$

708 Here the  $\mathbf{f}_{fric}$  stems from the soil-structure interaction following the contact  
 709 law between the soil/structure interfaces.

710 *Energy conservation*

711 We utilize the general form of the total energy balance equation for porous  
 712 media from [38]. The total energy balance equations for the fluid phases take  
 713 the following form:

$$\frac{1}{V} \frac{D_f(m_f(e_f + 0.5 \mathbf{U}_f^2))}{Dt} = \nabla \cdot (-np_f \mathbf{I}) \cdot \mathbf{U}_f + \nabla \cdot \mathbf{q}_f + (\bar{\rho}_f \mathbf{b}) \cdot \mathbf{U}_f + \sum \mathbf{f}_d \cdot \mathbf{U}_f + \sum q_{sf} \quad (114)$$

714 By applying the product rule  $D(m\mathbf{U}^2) = D(m\mathbf{U} \cdot \mathbf{U}) = 2\mathbf{U} \cdot D(m\mathbf{U})$ , we can  
 715 express the left-hand side of equation (114) as:

$$\frac{1}{V} \frac{D_f(m_f(e_f + 0.5 \mathbf{U}_f^2))}{Dt} = \frac{1}{V} \frac{D_f(m_f e_f)}{Dt} + \frac{1}{V} \frac{D_f(m_f \mathbf{U}_f)}{Dt} \cdot \mathbf{U}_f \quad (115)$$

716 Combining equations (111), (114), and (115), we derive the final form of the  
 717 internal energy balance equation for the fluid phases as:

$$\frac{1}{V} \frac{D_f(m_f e_f)}{Dt} = \frac{1}{V} \left[ \frac{\partial(m_f e_f)}{\partial t} + \nabla \cdot (m_f e_f \mathbf{U}_f) \right] = \bar{\rho}_f p_f \frac{D_f v_f}{Dt} + \nabla \cdot \mathbf{q}_f + \sum q_{sf} \quad (116)$$

718 On the right hand side, the terms include the average pressure-volume work,  
 719 the average viscous dissipation, the thermal transport and the energy ex-  
 720 change between solid and fluid respectively. The heat flux is  $\mathbf{q}_f = \bar{\rho}_f \beta_f \nabla T_f$

721 with  $\beta_f$  being the thermal conductivity coefficient. To derive the internal  
 722 energy balance equation for the solid phase, we introduce the rate of the  
 723 internal energy for the thermoelastic materials as a function of elastic strain  
 724 tensor  $\boldsymbol{\epsilon}_s^e$  and temperature  $T_s$  as belows:

$$\frac{m_s}{V} \frac{D_s(e_s)}{Dt} = \boldsymbol{\sigma}' : \frac{D_s(\boldsymbol{\epsilon}_s^e)}{Dt} + \frac{D_s(e_s)}{D_s(T_s)} \frac{D_s(T_s)}{Dt} = \boldsymbol{\sigma}' : \frac{D_s(\boldsymbol{\epsilon}_s^e)}{Dt} + c_v \frac{D_s(T_s)}{Dt} \quad (117)$$

725  $c_v$  is the specific heat at the constant volume of the solid materials. The total  
 726 energy balance equation for the mixture based on [38] can be written as:

$$\begin{aligned} 727 \quad & \frac{1}{V} \frac{D_f(m_f(e_f + 0.5\mathbf{U}_f^2))}{Dt} + \frac{1}{V} \frac{D_s(m_s(e_s + 0.5\mathbf{U}_s^2))}{Dt} = \nabla \cdot (-\phi_f p_f \mathbf{I}) \cdot \mathbf{U}_f \\ & + \nabla \cdot (\boldsymbol{\sigma}' - \phi_s p_f \mathbf{I}) \cdot \mathbf{U}_s + (-\phi_f p_f \mathbf{I}) : \nabla \mathbf{U}_f + \boldsymbol{\sigma}' : \nabla \mathbf{U}_s \\ & + (\bar{\rho}_f \mathbf{b}) \cdot \mathbf{U}_f + (\bar{\rho}_s \mathbf{b}) \cdot \mathbf{U}_s + \nabla \cdot \mathbf{q}_f + \nabla \cdot \mathbf{q}_s + \sum \mathbf{f}_d \cdot (\mathbf{U}_f - \mathbf{U}_s) \end{aligned} \quad (118)$$

728 Subtracting equation (118), (117) to equations (114) and (113), we obtained  
 729 the internal energy balance equation for solid phase as:

$$\boldsymbol{\sigma}' : \frac{D_s(\boldsymbol{\epsilon}_s^e)}{Dt} + \frac{m_s}{V} c_v \frac{D_s(T_s)}{Dt} = \Delta W_s + \Delta W_{friction} + \nabla \cdot \mathbf{q}_s - \sum q_{sf} \quad (119)$$

730 On the right hand side, the terms include the work rate from frictional sliding  
 731 between solid materials  $\Delta W_{friction}$ , thermal transport and energy exchange  
 732 between solid and fluid respectively. The heat flux is  $\mathbf{q}_s = \bar{\rho}_s \beta_s \nabla T_s$  with  $\beta_s$   
 733 being the thermal conductivity of the solid materials, the mechanical work  
 734 rate  $\Delta W_s = \boldsymbol{\sigma}' : \frac{D_s(\boldsymbol{\epsilon}_s)}{Dt} = \boldsymbol{\sigma}' : \left( \frac{D_s(\boldsymbol{\epsilon}_s^e)}{Dt} + \frac{D_s(\boldsymbol{\epsilon}_s^p)}{Dt} \right)$  computed from the constitutive  
 735 model with  $\boldsymbol{\epsilon}_s^p$  is the plastic strain tensor, . By subtracting the term  $\boldsymbol{\sigma}' : \frac{D_s(\boldsymbol{\epsilon}_s^e)}{Dt}$ ,  
 736 we get the final form of the energy balance equation as:

$$\frac{m_s}{V} c_v \frac{D_s(T_s)}{Dt} = \boldsymbol{\sigma}' : \frac{D_s(\boldsymbol{\epsilon}_s^p)}{Dt} + \Delta W_{friction} + \nabla \cdot \mathbf{q}_s - \sum q_{sf} \quad (120)$$

### 737 Advanced Fluid Pressure

738 The discretization of the pressure equation begins with the Lagrangian  
 739 cell face velocity and the equation for the pressure as:

$$\bar{\rho}_{f,FC} \frac{\mathbf{U}_{f,FC}^{n+1} - \mathbf{U}_{f,FC}^n}{dt} = n \nabla^{FC} P_{f,c}^{n+1} + \bar{\rho}_{f,FC} \mathbf{b} \quad (121)$$

740

$$\kappa \frac{dP}{dt} = \nabla^c \cdot \mathbf{U}_{f,FC}^{n+1} \quad (122)$$

741 The divergence of the equation (121) with  $\nabla \cdot \mathbf{b} = 0$  is:

$$\nabla^c \cdot \mathbf{U}_{f,FC}^{n+1} - \nabla^c \cdot \mathbf{U}_{f,FC}^n = \nabla^c \frac{\Delta t}{\rho_{f,FC}^n} \cdot \nabla^{FC} (P_{f,c}^n + \Delta P_{f,c}^n) \quad (123)$$

742 To solve this equation, we define the cell face intermediate velocity  $\mathbf{U}_{f,FC}^*$  as:

$$\bar{\rho}_{f,FC} \frac{\mathbf{U}_{f,FC}^* - \mathbf{U}_{f,FC}^n}{\Delta t} = n \nabla^{FC} P_{f,c}^n + \bar{\rho}_{f,FC} \mathbf{b} \quad (124)$$

743 The divergence of the equation (124) is:

$$\nabla^c \cdot \mathbf{U}_{f,FC}^* - \nabla^c \cdot \mathbf{U}_{f,FC}^n = \nabla^c \frac{\Delta t}{\rho_{f,FC}^n} \cdot \nabla^{FC} P_{f,c}^n \quad (125)$$

744 Combining equations (122, 123, 125), it leads to:

$$\left( \kappa - \nabla^c \frac{\Delta t}{\rho_{f,FC}^n} \cdot \nabla^{FC} \right) \Delta P_{fc}^n = -\nabla^c \cdot \mathbf{U}_{f,FC}^* \quad (126)$$

745 When the fluid is incompressible,  $\kappa$  approaches to zero and the equation  
746 (126) becomes the Poisson's equation for the incompressible fluid flow.

#### 747 *Momentum and Energy exchange with an implicit solver*

748 Considering the fluid momentum balance equation as:

$$(m\mathbf{U})_{f,FC}^{n+1} = (m\mathbf{U})_{f,FC}^n - \Delta t (Vn \nabla^{FC} P_{f,c}^n + m_f \mathbf{b}) + VK \Delta t (\mathbf{U}_{s,FC}^{n+1} - \mathbf{U}_{f,FC}^{n+1}) \quad (127)$$

749 And assuming  $m_{f,FC}^{n+1} = m_{f,FC}^n$ , we get:

$$\mathbf{U}_{f,FC}^{n+1} = \mathbf{U}_{f,FC}^n - \Delta t \left( \frac{\nabla^{FC} P_{fc}^n}{\rho_{f,FC}^n} + \mathbf{b} \right) + \frac{\Delta t K}{\rho_{f,FC}^n} (\mathbf{U}_{s,FC}^{n+1} - \mathbf{U}_{f,FC}^{n+1}) \quad (128)$$

750 As defined in the section 'Advanced Fluid Pressure', the cell face intermediate  
751 fluid velocity  $\mathbf{U}_{f,FC}^* = \Delta t (\nabla^{FC} P_{fc}^n / \rho_{f,FC}^n + \mathbf{b})$  is computed as:

$$\mathbf{U}_{f,FC}^{n+1} = \mathbf{U}_{f,FC}^* + \frac{\Delta t K}{\rho_{f,FC}^n} (\mathbf{U}_{s,FC}^{n+1} - \mathbf{U}_{f,FC}^{n+1}) \quad (129)$$

752 Considering the solid momentum balance equation as:

$$(m\mathbf{U})_{s,FC}^{n+1} = (m\mathbf{U})_{s,FC}^n - \Delta t(V\nabla^{FC} \cdot \boldsymbol{\sigma}'^n - V(1-n)\nabla^{FC}P_{f,c}^n + m_s\mathbf{b}) - VK\Delta t(\mathbf{U}_{s,FC}^{n+1} - \mathbf{U}_{f,FC}^{n+1}) \quad (130)$$

753 We define the cell face intermediate solid velocity as  $\mathbf{U}_{s,FC}^* = \Delta t(\nabla^{FC} \cdot$

754  $\boldsymbol{\sigma}_c'^n/\bar{\rho}_{s,FC} - \nabla^{FC}P_{f,c}^n/\rho_s + \mathbf{b})$  leading to:

$$\mathbf{U}_{s,FC}^{n+1} = \mathbf{U}_{s,FC}^* - \frac{\Delta t K}{\bar{\rho}_{s,FC}^n}(\mathbf{U}_{s,FC}^{n+1} - \mathbf{U}_{f,FC}^{n+1}) \quad (131)$$

755 Combining equation (129) and (131) we get:

$$\begin{aligned} \mathbf{U}_{f,FC}^* + \Delta\mathbf{U}_{f,FC} &= \mathbf{U}_{f,FC}^* + \frac{\Delta t K}{\bar{\rho}_{f,FC}^n}(\mathbf{U}_{s,FC}^* + \Delta\mathbf{U}_{s,FC} - \mathbf{U}_{f,FC}^* - \Delta\mathbf{U}_{f,FC}) \\ \mathbf{U}_{s,FC}^* + \Delta\mathbf{U}_{s,FC} &= \mathbf{U}_{s,FC}^* - \frac{\Delta t K}{\bar{\rho}_{s,FC}^n}(\mathbf{U}_{s,FC}^* + \Delta\mathbf{U}_{s,FC} - \mathbf{U}_{f,FC}^* - \Delta\mathbf{U}_{f,FC}) \end{aligned} \quad (132)$$

756 Rearranging the equation (132), it leads to the linear system of equations as  
757 belows:

$$\begin{vmatrix} (1 + \beta_{12,FC}) & -\beta_{12,FC} \\ -\beta_{21,FC} & (1 + \beta_{21,FC}) \end{vmatrix} \begin{vmatrix} \Delta\mathbf{U}_{f,FC} \\ \Delta\mathbf{U}_{s,FC} \end{vmatrix} = \begin{vmatrix} \beta_{12,FC}(\mathbf{U}_{s,FC}^* - \mathbf{U}_{f,FC}^*) \\ \beta_{21,FC}(\mathbf{U}_{f,FC}^* - \mathbf{U}_{s,FC}^*) \end{vmatrix}$$

758 Solving this linear equations with  $\beta_{12,FC} = (\Delta t K)/\bar{\rho}_{f,FC}^n$  and  $\beta_{21,FC} =$   
759  $(\Delta t K)/\bar{\rho}_{s,FC}^n$  with K is the momentum exchange coefficient. Similar derivation  
760 can be performed to computed the cell-center velocity increment leading  
761 to:

$$\begin{vmatrix} (1 + \beta_{12c}) & -\beta_{12c} \\ -\beta_{21c} & (1 + \beta_{21c}) \end{vmatrix} \begin{vmatrix} \Delta\mathbf{U}_{f,c} \\ \Delta\mathbf{U}_{sc} \end{vmatrix} = \begin{vmatrix} \beta_{12c}(\mathbf{U}_{sc}^* - \mathbf{U}_{f,c}^*) \\ \beta_{21c}(\mathbf{U}_{f,c}^* - \mathbf{U}_{sc}^*) \end{vmatrix}$$

762 with  $\beta_{12c} = (\Delta t K)/\bar{\rho}_{f,c}^n$  and  $\beta_{21c} = (\Delta t K)/\bar{\rho}_{sc}^n$  and the cell-centered interme-  
763 diate velocity can be calculated by:

$$\begin{aligned} \mathbf{U}_{f,c}^* &= \mathbf{U}_{f,c}^n + \Delta t\left(-\frac{\nabla P_{f,c}^{n+1}}{\bar{\rho}_{f,c}^n} + \frac{\nabla \cdot \boldsymbol{\tau}_{f,c}^n}{\bar{\rho}_{f,c}^n} + \mathbf{b}\right) \\ \mathbf{U}_{sc}^* &= \mathbf{U}_{sc}^n + \Delta t\left(\frac{\nabla \cdot \boldsymbol{\sigma}_c'^n}{\bar{\rho}_{sc}^n} - \frac{\nabla P_{f,c}^{n+1}}{\rho_s} + \mathbf{b}\right) \end{aligned} \quad (133)$$

764 For generalize multi materials i,j = 1:N, the linear equations is in the form

765 as:

$$\begin{vmatrix} (1 + \beta_{ij}) & -\beta_{ij} \\ -\beta_{ji} & (1 + \beta_{ji}) \end{vmatrix} \begin{vmatrix} \Delta\mathbf{U}_i \\ \Delta\mathbf{U}_j \end{vmatrix} = \begin{vmatrix} \beta_{ij}(\mathbf{U}_i^* - \mathbf{U}_j^*) \\ \beta_{ji}(\mathbf{U}_j^* - \mathbf{U}_i^*) \end{vmatrix}$$

766 Similar approach applied for the energy exchange term leading to:

$$\begin{vmatrix} (1 + \eta_{ij}) & -\eta_{ij} \\ -\eta_{ji} & (1 + \eta_{ji}) \end{vmatrix} \begin{vmatrix} \Delta T_i \\ \Delta T_j \end{vmatrix} = \begin{vmatrix} \eta_{ij}(T_i^n - T_j^n) \\ \eta_{ji}(T_j^n - T_i^n) \end{vmatrix}$$

767 with  $\eta$  is the energy exchange coefficient.

## 768 References

- 769 [1] D. Yuk, S. Yim, P.-F. Liu, Numerical modeling of submarine mass-  
770 movement generated waves using RANS model, Computers and Geo-  
771 sciences 32 (7) (2006) 927–935. doi:10.1016/j.cageo.2005.10.028.  
772 URL <https://doi.org/10.1016/j.cageo.2005.10.028>
- 773 [2] S. Glimsdal, J.-S. L'Heureux, C. B. Harbitz, F. Løvholt, The 29th jan-  
774 uary 2014 submarine landslide at statland, norway—landslide dynamics,  
775 tsunami generation, and run-up, Landslides 13 (6) (2016) 1435–1444.  
776 doi:10.1007/s10346-016-0758-7.  
777 URL <https://doi.org/10.1007/s10346-016-0758-7>
- 778 [3] S. Abadie, D. Morichon, S. Grilli, S. Glockner, Numerical sim-  
779 ulation of waves generated by landslides using a multiple-fluid  
780 navier–stokes model, Coastal Engineering 57 (9) (2010) 779–794.  
781 doi:10.1016/j.coastaleng.2010.03.003.  
782 URL <https://doi.org/10.1016/j.coastaleng.2010.03.003>
- 783 [4] M. Rauter, S. Viroulet, S. S. Gylfadóttir, W. Fellin, F. Løvholt, Granular  
784 porous landslide tsunami modelling – the 2014 lake askja flank collapse,  
785 Nature Communications 13 (1) (Feb. 2022). doi:10.1038/s41467-022-  
786 28296-7.  
787 URL <https://doi.org/10.1038/s41467-022-28296-7>
- 788 [5] Q.-A. Tran, W. Sołowski, Generalized interpolation material point  
789 method modelling of large deformation problems including strain-  
790 rate effects – application to penetration and progressive fail-  
791 ure problems, Computers and Geotechnics 106 (2019) 249–265.  
792 doi:10.1016/j.compgeo.2018.10.020.  
793 URL <https://doi.org/10.1016/j.compgeo.2018.10.020>

- 794 [6] T. Capone, A. Panizzo, J. J. Monaghan, SPH modelling of water  
795 waves generated by submarine landslides, *Journal of Hydraulic Research*  
796 48 (sup1) (2010) 80–84. doi:10.1080/00221686.2010.9641248.  
797 URL <https://doi.org/10.1080/00221686.2010.9641248>
- 798 [7] X. Zhang, E. Oñate, S. A. G. Torres, J. Bleyer, K. Krabbenhoft, A  
799 unified lagrangian formulation for solid and fluid dynamics and its possi-  
800 bility for modelling submarine landslides and their consequences, *Computer  
801 Methods in Applied Mechanics and Engineering* 343 (2019) 314–  
802 338. doi:10.1016/j.cma.2018.07.043.  
803 URL <https://doi.org/10.1016/j.cma.2018.07.043>
- 804 [8] R. Dey, B. C. Hawlader, R. Phillips, K. Soga, Numerical modelling  
805 of submarine landslides with sensitive clay layers, *Géotechnique* 66 (6)  
806 (2016) 454–468. doi:10.1680/jgeot.15.p.111.  
807 URL <https://doi.org/10.1680/jgeot.15.p.111>
- 808 [9] S. Bandara, K. Soga, Coupling of soil deformation and pore fluid flow  
809 using material point method, *Computers and Geotechnics* 63 (2015)  
810 199–214. doi:10.1016/j.compgeo.2014.09.009.  
811 URL <https://doi.org/10.1016/j.compgeo.2014.09.009>
- 812 [10] A. P. Tampubolon, T. Gast, G. Klár, C. Fu, J. Teran, C. Jiang,  
813 K. Museth, Multi-species simulation of porous sand and water  
814 mixtures, *ACM Transactions on Graphics* 36 (4) (2017) 1–11.  
815 doi:10.1145/3072959.3073651.  
816 URL <https://doi.org/10.1145/3072959.3073651>
- 817 [11] A. S. Baumgarten, K. Kamrin, A general constitutive model for dense,  
818 fine-particle suspensions validated in many geometries, *Proceedings  
819 of the National Academy of Sciences* 116 (42) (2019) 20828–20836.  
820 doi:10.1073/pnas.1908065116.  
821 URL <https://doi.org/10.1073/pnas.1908065116>
- 822 [12] Q.-A. Tran, W. Sołowski, Temporal and null-space filter for the ma-  
823 terial point method, *International Journal for Numerical Methods in  
824 Engineering* 120 (3) (2019) 328–360. doi:10.1002/nme.6138.  
825 URL <https://doi.org/10.1002/nme.6138>

- 826 [13] X. Zheng, F. Pisanò, P. J. Vardon, M. A. Hicks, An explicit stabilised  
827 material point method for coupled hydromechanical problems in two-  
828 phase porous media, *Computers and Geotechnics* 135 (2021) 104112.  
829 doi:10.1016/j.compgeo.2021.104112.  
830 URL <https://doi.org/10.1016/j.compgeo.2021.104112>
- 831 [14] Q. A. Tran, W. Sołowski, M. Berzins, J. Guilkey, A convected particle  
832 least square interpolation material point method, *International Journal*  
833 for Numerical Methods in Engineering
- 834 121 (6) (2019) 1068–1100.  
835 doi:10.1002/nme.6257.  
URL <https://doi.org/10.1002/nme.6257>
- 836 [15] J. Zhao, T. Shan, Coupled cfd–dem simulation of fluid–particle in-  
837 teraction in geomechanics, *Powder Technology* 239 (2013) 248–258.  
838 doi:<https://doi.org/10.1016/j.powtec.2013.02.003>.  
839 URL <https://www.sciencedirect.com/science/article/pii/S0032591013001113>
- 840 [16] T. Shan, J. Zhao, A coupled cfd-dem analysis of granular flow im-  
841 pacting on a water reservoir, *Acta Mechanica* 225 (2014) 2449–2470.  
842 doi:<https://doi.org/10.1007/s00707-014-1119-z>.
- 843 [17] S. Zhao, J. Zhao, W. Liang, F. Niu, Multiscale modeling of coupled  
844 thermo-mechanical behavior of granular media in large deforma-  
845 tion and flow, *Computers and Geotechnics* 149 (2022) 104855.  
846 doi:<https://doi.org/10.1016/j.compgeo.2022.104855>.  
847 URL <https://www.sciencedirect.com/science/article/pii/S0266352X22002038>
- 848 [18] S. Zhao, H. Chen, J. Zhao, Multiscale modeling of freeze-thaw be-  
849 havior in granular media, *Acta Mechanica Sinica* 37 (2023) 722195.  
850 doi:<https://doi.org/10.1007/s10409-022-22195-x>.
- 851 [19] N. M. Pinyol, M. Alvarado, E. E. Alonso, F. Zabala,  
852 Thermal effects in landslide mobility, *Géotechnique* 68 (6)  
853 (2018) 528–545. arXiv:<https://doi.org/10.1680/jgeot.17.P.054>,  
854 doi:10.1680/jgeot.17.P.054.  
855 URL <https://doi.org/10.1680/jgeot.17.P.054>
- 856 [20] J.-S. Chen, M. Hillman, S.-W. Chi, Meshfree methods: Progress made  
857 after 20 years, *Journal of Engineering Mechanics* 143 (4) (Apr. 2017).

- 858                   doi:10.1061/(asce)em.1943-7889.0001176.  
 859                   URL [https://doi.org/10.1061/\(asce\)em.1943-7889.0001176](https://doi.org/10.1061/(asce)em.1943-7889.0001176)
- 860 [21] F. H. Harlow, A. A. Amsden, Numerical calculation of almost incom-  
 861 pressible flow, *Journal of Computational Physics* 3 (1) (1968) 80–93.  
 862 doi:[https://doi.org/10.1016/0021-9991\(68\)90007-7](https://doi.org/10.1016/0021-9991(68)90007-7).  
 863 URL <https://www.sciencedirect.com/science/article/pii/0021999168900077>
- 864 [22] B. A. Kashiwa, A multifield model and method for fluid-structure in-  
 865 teraction dynamics, *Tech. Rep. LA-UR-01-1136*, Los Alamos National  
 866 Laboratory (2001).
- 867 [23] J. Guilkey, T. Harman, B. Banerjee, An eulerian-lagrangian  
 868 approach for simulating explosions of energetic devices,  
 869 *Computers and Structures* 85 (11) (2007) 660 – 674.  
 870 doi:<https://doi.org/10.1016/j.compstruc.2007.01.031>.  
 871 URL <http://www.sciencedirect.com/science/article/pii/S0045794907000429>
- 872 [24] A. S. Baumgarten, B. L. Couchman, K. Kamrin, A coupled finite volume  
 873 and material point method for two-phase simulation of liquid-sediment  
 874 and gas-sediment flows, *Computer Methods in Applied Mechanics and*  
 875 *Engineering* 384 (2021) 113940. doi:10.1016/j.cma.2021.113940.  
 876 URL <https://doi.org/10.1016/j.cma.2021.113940>
- 877 [25] J. Clausen, L. Damkilde, L. Andersen, Efficient return algorithms for  
 878 associated plasticity with multiple yield planes, *International Journal*  
 879 *for Numerical Methods in Engineering* 66 (6) (2006) 1036–1059.  
 880 arXiv:<https://onlinelibrary.wiley.com/doi/pdf/10.1002/nme.1595>,  
 881 doi:<https://doi.org/10.1002/nme.1595>.  
 882 URL <https://onlinelibrary.wiley.com/doi/abs/10.1002/nme.1595>
- 883 [26] P. Moin, K. Squires, W. Cabot, S. Lee, A dynamic  
 884 subgrid-scale model for compressible turbulence and scalar  
 885 transport, *Physics of Fluids A: Fluid Dynamics* 3 (11)  
 886 (1991) 2746–2757. arXiv:[https://pubs.aip.org/aip/pof/article-pdf/3/11/2746/12328150/2746\\_1\\_online.pdf](https://pubs.aip.org/aip/pof/article-pdf/3/11/2746/12328150/2746_1_online.pdf), doi:10.1063/1.858164.  
 887 URL <https://doi.org/10.1063/1.858164>
- 889 [27] S. Bardenhagen, J. Guilkey, K. Roessig, J. Brackbill, W. Witzel,  
 890 J.C.Foster, An improved contact algorithm for the material point

- method and application to stress propagation in granular material, CMES-Computer Modeling in Engineering and Sciences 2 (2001) 509–522. doi:10.3970/cmes.2001.002.509.
- [28] J. A. M. K. R. Beetstra, M. A. van der Hoef, Drag force of intermediate reynolds number flow past mono- and bidisperse arrays of spheres, Fluid Mechanics and Transport Phenomena 53 (2) (2007) 489 – 501. doi:<https://doi.org/10.1002/aic.11065>.
- [29] R. W. Stewart, The air-sea momentum exchange, Boundary-Layer Meteorology 6 (1-2) (1974) 151–167. doi:10.1007/bf00232481.  
URL <https://doi.org/10.1007/bf00232481>
- [30] S. G. Bardenhagen, E. M. Kober, The generalized interpolation material point method, Computer Modeling in Engineering and Sciences 5 (2004) 477–496. doi:10.1016/j.compgeo.2021.104199.  
URL <https://doi.org/10.3970/cmes.2004.005.477>
- [31] S. G. Amiri, E. Taheri, A. Lavasan, A hybrid finite element model for non-isothermal two-phase flow in deformable porous media, Computers and Geotechnics 135 (2021) 104199. doi:10.1016/j.compgeo.2021.104199.  
URL <https://doi.org/10.1016/j.compgeo.2021.104199>
- [32] S. A. R. C. Mariotti;, P. Heinrich, Numerical simulation of submarine landslides and their hydraulic effects, Journal of Waterway, Port, Coastal, and Ocean Engineering 123 (4) (1997). doi:[https://doi.org/10.1061/\(ASCE\)0733-950X\(1997\)123:4\(149\)](https://doi.org/10.1061/(ASCE)0733-950X(1997)123:4(149)).
- [33] A. Alsardi, A. Yerro, Runout Modeling of Earthquake-Triggered Landslides with the Material Point Method, pp. 21–31. arXiv:<https://ascelibrary.org/doi/pdf/10.1061/9780784483428.003>, doi:10.1061/9780784483428.003.  
URL <https://ascelibrary.org/doi/abs/10.1061/9780784483428.003>
- [34] H. N., O. A., B. H. H., R. P., R. Fukagawa, Seismic slope failuremodelling using the mesh-free sph method, International Journal of Geomate (2013) 660–665.
- [35] T. Bhandari, F. Hamad, C. Moormann, K. Sharma, B. Westrich, Numerical modelling of seismic slope failure using mpm, Computers and Geotechnics 75 (2016) 126–134.

- 924 doi:<https://doi.org/10.1016/j.compgeo.2016.01.017>.  
925 URL <https://www.sciencedirect.com/science/article/pii/S0266352X16000264>
- 926 [36] D. Muir Wood, Soil behaviour and critical state soil mechanics, Cam-  
927 bridge University Press, United Kingdom, 1990.
- 928 [37] D. Drumheller, On theories for reacting immiscible mixtures, Inter-  
929 national Journal of Engineering Science 38 (3) (2000) 347 – 382.  
930 doi:[https://doi.org/10.1016/S0020-7225\(99\)00047-6](https://doi.org/10.1016/S0020-7225(99)00047-6).  
931 URL <http://www.sciencedirect.com/science/article/pii/S0020722599000476>
- 932 [38] S. Hassanzadeh, Derivation of basic equations of mass transport in  
933 porous media, part1: Macroscopic balance laws, Advances in Wa-  
934 ter Resources 9 (1986) 196–206. doi:[https://doi.org/10.1016/0309-1708\(86\)90024-2](https://doi.org/10.1016/0309-1708(86)90024-2).  
935